

Coupled spin-orbital fluctuations in a three orbital model for $4d$ and $5d$ oxides with electron fillings $n = 3, 4, 5$ — Application to NaOsO_3 , Ca_2RuO_4 , and Sr_2IrO_4

Shubhajyoti Mohapatra and Avinash Singh*

Department of Physics, Indian Institute of Technology, Kanpur - 208016, India

(Dated: February 1, 2022)

A unified approach is presented for investigating coupled spin-orbital fluctuations within a realistic three-orbital model for strongly spin-orbit coupled systems with electron fillings $n = 3, 4, 5$ in the t_{2g} sector of d_{yz}, d_{xz}, d_{xy} orbitals. A generalized fluctuation propagator is constructed which is consistent with the generalized self-consistent Hartree-Fock approximation where all Coulomb interaction contributions involving orbital diagonal and off-diagonal spin and charge condensates are included. Besides the low-energy magnon, intermediate-energy orbiton and spin-orbiton, and high-energy spin-orbit exciton modes, the generalized spectral function also shows other high-energy excitations such as the Hund's coupling induced gapped magnon modes. We relate the characteristic features of the coupled spin-orbital excitations to the complex magnetic behavior resulting from the interplay between electronic bands, spin-orbit coupling, Coulomb interactions, and structural distortion effects, as realized in the compounds NaOsO_3 , Ca_2RuO_4 , and Sr_2IrO_4 .

I. INTRODUCTION

The $4d$ and $5d$ transition metal (TM) oxides exhibit an unprecedented coupling between spin, charge, orbital, and structural degrees of freedom. The complex interplay between the different physical elements such as strong spin-orbit coupling (SOC), Coulomb interactions, and structural distortions results in novel magnetic states and unconventional collective excitations.^{1–6} In particular, the cubic structured NaOsO_3 and perovskite structured Ca_2RuO_4 and Sr_2IrO_4 compounds, corresponding to d^n electronic configuration of the TM ion with electron fillings $n=3,4,5$ in the t_{2g} sector, respectively, are at the emerging research frontier as they provide versatile platform for the exploration of SOC-driven phenomena involving collective electronic and magnetic behavior including coupled spin-orbital excitations.

The different physical elements give rise to a rich variety of nontrivial microscopic features which contribute to the complex interplay. These include spin-orbital-entangled states, band narrowing, spin-orbit gap, and explicit spin-rotation-symmetry breaking (due to SOC), electronic band narrowing due to reduced effective hopping (octahedral tilting and rotation), crystal field induced tetragonal splitting (octahedral compression), orbital mixing (SOC and octahedral tilting, rotation) which self consistently generates induced SOC terms and orbital moment interaction from the Coulomb interaction terms, significantly weaker electron correlation term U compared to $3d$ orbitals and therefore critical contribution of Hund's coupling to local magnetic moment. These microscopic features contribute to the complex interplay in different ways for electron fillings $n=3,4,5$, resulting in significantly different macroscopic properties of the three compounds, which are briefly reviewed below along with experimental observations about the collective and coupled spin-orbital excitations as obtained from recent resonant inelastic X-ray scattering (RIXS) studies.

The nominally orbitally quenched d^3 compound NaOsO_3 undergoes a metal-insulator transition (MIT) ($T_{\text{MI}} = T_{\text{N}} = 410$ K) that is closely related to the onset of long-range antiferromagnetic (AFM) order.^{7–10} Various mechanisms, such as Slater-like, magnetic Lifshitz transition, and AFM band insulator have been proposed to explain this unusual and intriguing nature of the MIT.^{8,11–14} Interplay of electronic correlations, Hund's coupling, and octahedral tilting and rotation induced band narrowing near the Fermi level in this weakly correlated compound results in the weakly insulating state with G-type AFM or-

der, with magnetic anisotropy and large magnon gap resulting from interplay of SOC, band structure, and the tetragonal splitting.^{14,15} The Os L_3 resonant edge RIXS measurements at room temperature show four inelastic peak features below 1.5 eV, which have been interpreted to correspond to the strongly gapped (~ 58 meV) dispersive magnon excitations with bandwidth ~ 100 meV, excitations (centered at ~ 1 eV) within the t_{2g} manifold, and excitations from t_{2g} to e_g states and ligand-to-metal charge transfer for the remaining two higher-energy peaks.^{13,16,17} The intensity and positions of the three high-energy peaks appear to be essentially temperature independent.

The nominally spin $S=1$ d^4 compound Ca_2RuO_4 undergoes a MIT at $T_{\text{MI}}=357$ K and magnetic transition at $T_{\text{N}}=110$ K ($\ll T_{\text{MI}}$) via a structural phase transition involving a compressive tetragonal distortion, tilt, and rotation of the RuO_6 octahedra.^{18–21} The low-temperature AFM insulating phase is thus characterized by highly distorted octahedra with nominally filled xy orbital and half-filled yz, xz orbitals.^{22–24} This transition has also been identified in pressure,^{25–27} chemical substitution,^{28–30} strain,³¹ and electrical current studies,^{32,33} and highlights the complex interplay between SOC, Coulomb interactions, and structural distortions.

Inelastic neutron scattering (INS)^{34–36} and Raman³⁷ studies on Ca_2RuO_4 have revealed unconventional low-energy (~ 50 and 80 meV) excitations interpreted as gapped transverse magnon modes and possibly soft longitudinal (“Higgs-like”) or two-magnon excitation modes. From both Ru L_3 -edge and oxygen K -edge RIXS studies, multiple nontrivial excitations within the t_{2g} manifold were observed recently below 1 eV.^{38–40} Two low-energy (~ 80 and 350 meV) and two high-energy (~ 750 meV and 1 eV) excitations were identified within the limited energy resolution of RIXS. From the incident angle and polarisation dependence of the RIXS spectra, the orbital character of the 80 meV peak was inferred to be mixture of xy and xz/yz states, whereas the 0.4 eV peak was linked to unoccupied xz/yz states. Guided by phenomenological spin models, the low-energy excitations (consisting of multiple branches) were interpreted as composite spin-orbital excitations (also termed as “spin orbitons”).

Finally, SOC induced novel Mott insulating state is realized in the d^5 compound Sr_2IrO_4 ,^{41,42} where band narrowing of the spin-orbital-entangled electronic states near the Fermi level plays a critical role in the insulating behavior. The AFM insulating ground state is characterized by the correlation induced insulating gap within the nominally $J=1/2$

bands emerging from the Kramers doublet, which are separated from the bands of the $J=3/2$ quartet by energy $3\lambda/2$, where λ is the SOC strength. The RIXS spectra show low-energy dispersive magnon excitations (up to 200 meV), further resolved into two gapped magnon modes with energy gaps ~ 40 meV and 3 meV at the Γ point corresponding to out-of-plane and in-plane fluctuation modes, respectively.^{43–46} Weak electron correlation effect and mixing between the $J=1/2$ and $3/2$ sectors were identified as contributing significantly to the strong zone-boundary magnon dispersion as measured in RIXS studies.⁴⁷ In addition, high-energy dispersive spin-orbit exciton modes have also been revealed in RIXS studies in the energy range 0.4–0.8 eV.⁴⁸ This distinctive mode is also referred to as the spin-orbiton mode,^{49,50} and has been attributed to the correlated motion of electron-hole pair excitations across the renormalized spin-orbit gap between the $J=1/2$ and $3/2$ bands.⁵¹

Most of the theoretical studies involving magnetic anisotropy effects and excitations in above systems have mainly focused on phenomenological spin models with different exchange interactions obtained as fitting parameters to the experimental spectra. However, the interpretation of experimental data remains incomplete since the character of the effective spins, the microscopic origin of their interactions, and the microscopic nature of the magnetic excitations are still debated.^{2–6} Realistic information about the spin-orbital character of both low and high-energy collective excitations, as inferred from the study of coupled spin-orbital excitations, is clearly important since the spin and orbital degrees of freedom are explicitly coupled, and both are controlled by the different physical elements such as SOC, Coulomb interaction terms, tetragonal compression induced crystal-field splitting between xy and yz, xz orbitals, octahedral tilting and rotation induced orbital mixing hopping terms, and band physics.

Due to the intimately intertwined roles of the different physical elements, a unified approach is therefore required for the realistic modeling of these systems in which all physical elements are treated on an equal footing. The generalized self-consistent approximation applied recently to the $n = 4$ compound Ca_2RuO_4 provides such a unified approach.⁵² Involving the self-consistent determination of magnetic order within a three-orbital interacting electron model including all orbital-diagonal and off-diagonal spin and charge condensates generated by the different Coulomb interaction terms, this approach explicitly incorporates the complex interplay and accounts for the observed behavior including the tetragonal distortion induced magnetic reorientation transition, orbital moment interaction induced orbital gap,

SOC and octahedral tilting induced easy-axis anisotropy, and Coulomb interaction induced anisotropic SOC renormalization. Extension to the $n = 5$ compound Sr_2IrO_4 ,⁵³ provides confirmation of the Hund's coupling induced easy-plane magnetic anisotropy, which is responsible for the ~ 40 meV magnon gap measured for the out-of-plane fluctuation mode.⁴⁶

Towards a generalized non-perturbative formalism unifying the magnetic order and anisotropy effects on one hand and collective excitations on the other, the natural extension of the above generalized condensate approach is therefore to consider the generalized fluctuation propagator in terms of the generalized spin $(\psi_\mu^\dagger[\sigma^\alpha]\psi_\nu)$ and charge $(\psi_\mu^\dagger[\mathbf{1}]\psi_\nu)$ operators in the pure spin-orbital basis of the t_{2g} orbitals $\mu, \nu = yz, xz, xy$ and spin components $\alpha = x, y, z$. The generalized operators include the normal ($\mu = \nu$) spin and charge operators as well as the orbital off-diagonal ($\mu \neq \nu$) cases which are related to the generalized spin-orbit coupling terms $(L_\alpha S_\beta)$, where $\alpha, \beta = x, y, z$ and the orbital angular momentum operators L_α . Constructing the generalized fluctuation propagator as above will ensure that this scheme is fully consistent with the generalized self-consistent approach involving the generalized condensates.

The different components of the generalized fluctuation propagator will therefore naturally include spin-orbitons and orbitons, corresponding to the spin-orbital $(L_\alpha S_\beta)$ and orbital (L_α) moment fluctuations, besides the normal spin and charge fluctuations. The normal spin fluctuations will include in-phase and out-of phase fluctuations with respect to different orbitals, the latter being strongly gapped due to Hund's coupling. The spin-orbitons will include the spin-orbit excitons measured in RIXS studies of Sr_2IrO_4 .

The structure of this paper is as below. The three-orbital model within the t_{2g} sector (including SOC, hopping, Coulomb interaction, and structural distortion terms), and the generalized self-consistent formalism including orbital diagonal and off-diagonal condensates are reviewed in Sec. II and III. After introducing the generalized fluctuation propagator in Sec. IV, results of the calculated fluctuation spectral functions are presented for the cases $n = 3, 4, 5$ (corresponding to the three compounds NaOsO_3 , Ca_2RuO_4 , Sr_2IrO_4) in Sections V, VI, VII. Finally, conclusions are presented in Sec. VIII. The basis-resolved contributions to the total spectral function showing the detailed spin-orbital character of the collective excitations are presented in the Appendix.

II. THREE ORBITAL MODEL WITH SOC AND COULOMB INTERACTIONS

In the three-orbital ($\mu = yz, xz, xy$), two-spin ($\sigma = \uparrow, \downarrow$) basis defined with respect to a common spin-orbital coordinate axes (Fig. 1), we consider the Hamiltonian $\mathcal{H} = \mathcal{H}_{\text{band}} + \mathcal{H}_{\text{cf}} + \mathcal{H}_{\text{int}} + \mathcal{H}_{\text{SOC}}$ within the t_{2g} manifold. For the band and crystal field terms together, we consider:

$$\mathcal{H}_{\text{band+cf}} = \sum_{\mathbf{k}\sigma s} \psi_{\mathbf{k}\sigma s}^\dagger \left[\begin{pmatrix} \epsilon_{\mathbf{k}}^{yz'} & 0 & 0 \\ 0 & \epsilon_{\mathbf{k}}^{xz'} & 0 \\ 0 & 0 & \epsilon_{\mathbf{k}}^{xy'} + \epsilon_{xy} \end{pmatrix} \delta_{ss'} + \begin{pmatrix} \epsilon_{\mathbf{k}}^{yz} & \epsilon_{\mathbf{k}}^{yz|xz} & \epsilon_{\mathbf{k}}^{yz|xy} \\ -\epsilon_{\mathbf{k}}^{yz|xz} & \epsilon_{\mathbf{k}}^{xz} & \epsilon_{\mathbf{k}}^{xz|xy} \\ -\epsilon_{\mathbf{k}}^{yz|xy} & -\epsilon_{\mathbf{k}}^{xz|xy} & \epsilon_{\mathbf{k}}^{xy} \end{pmatrix} \delta_{\bar{s}s'} \right] \psi_{\mathbf{k}\sigma s'} \quad (1)$$

in the composite three-orbital, two-sublattice ($s, s' = A, B$) basis. Here the energy offset ϵ_{xy} (relative to the degenerate yz/xz orbitals) represents the tetragonal distortion induced crystal field effect. The band dispersion terms in the two groups correspond to hopping terms connecting the same and opposite sublattice(s), and are given by:

$$\begin{aligned} \epsilon_{\mathbf{k}}^{xy} &= -2t_1(\cos k_x + \cos k_y) \\ \epsilon_{\mathbf{k}}^{xy'} &= -4t_2 \cos k_x \cos k_y - 2t_3(\cos 2k_x + \cos 2k_y) \\ \epsilon_{\mathbf{k}}^{yz} &= -2t_5 \cos k_x - 2t_4 \cos k_y \\ \epsilon_{\mathbf{k}}^{xz} &= -2t_4 \cos k_x - 2t_5 \cos k_y \\ \epsilon_{\mathbf{k}}^{yz|xz} &= -2t_{m1}(\cos k_x + \cos k_y) \\ \epsilon_{\mathbf{k}}^{xz|xy} &= -2t_{m2}(2 \cos k_x + \cos k_y) \\ \epsilon_{\mathbf{k}}^{yz|xy} &= -2t_{m3}(\cos k_x + 2 \cos k_y). \end{aligned} \quad (2)$$

Here t_1, t_2, t_3 are respectively the first, second, and third neighbor hopping terms for the xy orbital. For the yz (xz) orbital, t_4 and t_5 are the nearest-neighbor (NN) hopping terms in y (x) and x (y) directions, respectively, corresponding to π and δ orbital overlaps. Octahedral rotation and tilting induced orbital mixings are represented by the NN hopping terms t_{m1} (between yz and xz) and t_{m2}, t_{m3} (between xy and xz, yz). In the $n = 4$ case corresponding to the Ca_2RuO_4 compound, we have taken hopping parameter values: $(t_1, t_2, t_3, t_4, t_5) = (-1.0, 0.5, 0, -1.0, 0.2)$, orbital mixing hopping terms: $t_{m1} = 0.2$ and $t_{m2} = t_{m3} = 0.15$ ($\approx 0.2/\sqrt{2}$), and $\epsilon_{xy} = -0.8$, all in units of the realistic hopping energy scale $|t_1| = 150$ meV.^{54–56} The choice $t_{m2} = t_{m3}$ corresponds to the octahedral tilting axis oriented along

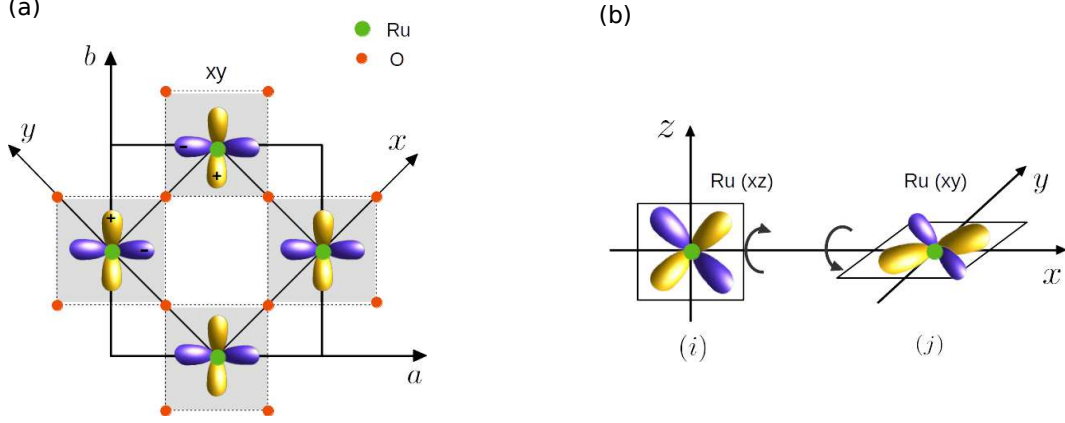


FIG. 1: (a) The common spin-orbital coordinate axes ($x-y$) along the Ru-O-Ru directions, shown along with the crystal axes a, b . (b) Octahedral tilting about the crystal a axis is resolved along the x, y axes, resulting in orbital mixing hopping terms between the xy and yz, xz orbitals.

the $\pm(-\hat{x} + \hat{y})$ direction, which is equivalent to the crystal $\mp a$ direction (Fig. 1). The t_{m1} and $t_{m2,m3}$ values taken above approximately correspond to octahedral rotation and tilting angles of about 12° (≈ 0.2 rad) as reported in experimental studies.²⁶

For the on-site Coulomb interaction terms in the t_{2g} basis ($\mu, \nu = yz, xz, xy$), we consider:

$$\begin{aligned}
 \mathcal{H}_{\text{int}} &= U \sum_{i,\mu} n_{i\mu\uparrow} n_{i\mu\downarrow} + U' \sum_{i,\mu<\nu,\sigma} n_{i\mu\sigma} n_{i\nu\bar{\sigma}} + (U' - J_H) \sum_{i,\mu<\nu,\sigma} n_{i\mu\sigma} n_{i\nu\sigma} \\
 &+ J_H \sum_{i,\mu\neq\nu} a_{i\mu\uparrow}^\dagger a_{i\nu\downarrow}^\dagger a_{i\mu\downarrow} a_{i\nu\uparrow} + J_P \sum_{i,\mu\neq\nu} a_{i\mu\uparrow}^\dagger a_{i\mu\downarrow}^\dagger a_{i\nu\downarrow} a_{i\nu\uparrow} \\
 &= U \sum_{i,\mu} n_{i\mu\uparrow} n_{i\mu\downarrow} + U'' \sum_{i,\mu<\nu} n_{i\mu} n_{i\nu} - 2J_H \sum_{i,\mu<\nu} \mathbf{S}_{i\mu} \cdot \mathbf{S}_{i\nu} + J_P \sum_{i,\mu\neq\nu} a_{i\mu\uparrow}^\dagger a_{i\mu\downarrow}^\dagger a_{i\nu\downarrow} a_{i\nu\uparrow} \quad (3)
 \end{aligned}$$

including the intra-orbital (U) and inter-orbital (U') density interaction terms, the Hund's coupling term (J_H), and the pair hopping interaction term (J_P), with $U'' \equiv U' - J_H/2 = U - 5J_H/2$ from the spherical symmetry condition $U' = U - 2J_H$. Here $a_{i\mu\sigma}^\dagger$ and $a_{i\mu\sigma}$ are the electron creation and annihilation operators for site i , orbital μ , spin $\sigma = \uparrow, \downarrow$. The density operator $n_{i\mu\sigma} = a_{i\mu\sigma}^\dagger a_{i\mu\sigma}$, total density operator $n_{i\mu} = n_{i\mu\uparrow} + n_{i\mu\downarrow} = \psi_{i\mu}^\dagger \psi_{i\mu}$, and spin density operator $\mathbf{S}_{i\mu} = \psi_{i\mu}^\dagger \boldsymbol{\sigma} \psi_{i\mu}$ in terms of the electron field operator $\psi_{i\mu}^\dagger = (a_{i\mu\uparrow}^\dagger \ a_{i\mu\downarrow}^\dagger)$. All interaction terms above are SU(2) invariant and thus possess spin rotation symmetry.

Finally, for the bare spin-orbit coupling term (for site i), we consider the spin-space

representation:

$$\begin{aligned}
\mathcal{H}_{\text{SOC}}(i) &= -\lambda \mathbf{L} \cdot \mathbf{S} = -\lambda (L_z S_z + L_x S_x + L_y S_y) \\
&= \left[\begin{pmatrix} \psi_{yz\uparrow}^\dagger & \psi_{yz\downarrow}^\dagger \end{pmatrix} (i\sigma_z \lambda/2) \begin{pmatrix} \psi_{xz\uparrow} \\ \psi_{xz\downarrow} \end{pmatrix} + \begin{pmatrix} \psi_{xz\uparrow}^\dagger & \psi_{xz\downarrow}^\dagger \end{pmatrix} (i\sigma_x \lambda/2) \begin{pmatrix} \psi_{xy\uparrow} \\ \psi_{xy\downarrow} \end{pmatrix} \right. \\
&\quad \left. + \begin{pmatrix} \psi_{xy\uparrow}^\dagger & \psi_{xy\downarrow}^\dagger \end{pmatrix} (i\sigma_y \lambda/2) \begin{pmatrix} \psi_{yz\uparrow} \\ \psi_{yz\downarrow} \end{pmatrix} \right] + \text{H.c.}
\end{aligned} \tag{4}$$

which explicitly breaks SU(2) spin rotation symmetry and therefore generates anisotropic magnetic interactions from its interplay with other Hamiltonian terms. Here we have used the matrix representation:

$$L_z = \begin{pmatrix} 0 & -i & 0 \\ i & 0 & 0 \\ 0 & 0 & 0 \end{pmatrix}, \quad L_x = \begin{pmatrix} 0 & 0 & 0 \\ 0 & 0 & -i \\ 0 & i & 0 \end{pmatrix}, \quad L_y = \begin{pmatrix} 0 & 0 & i \\ 0 & 0 & 0 \\ -i & 0 & 0 \end{pmatrix}, \tag{5}$$

for the orbital angular momentum operators in the three-orbital (yz, xz, xy) basis.

As the orbital “hopping” terms in Eq. (4) have the same form as spin-dependent hopping terms $i\sigma \cdot \mathbf{t}'_{ij}$, carrying out the strong-coupling expansion⁵⁷ for the $-\lambda L_z S_z$ term to second order in λ yields the anisotropic diagonal (AD) intra-site interactions:

$$[H_{\text{eff}}^{(2)}]_{\text{AD}}^{(z)}(i) = \frac{4(\lambda/2)^2}{U} [S_{yz}^z S_{xz}^z - (S_{yz}^x S_{xz}^x + S_{yz}^y S_{xz}^y)] \tag{6}$$

between yz, xz moments if these orbitals are nominally half-filled, as in the case of Ca_2RuO_4 . This term explicitly yields preferential $x - y$ plane ordering (easy-plane anisotropy) for parallel yz, xz moments, as enforced by the relatively stronger Hund’s coupling.

Similarly, from the strong coupling expansion for the other two SOC terms, we obtain additional anisotropic interaction terms which are shown below to yield C_4 symmetric easy-axis anisotropy within the easy plane. From the $-\lambda L_x S_x$ and $-\lambda L_y S_y$ terms, we obtain:

$$\begin{aligned}
[H_{\text{eff}}^{(2)}]_{\text{AD}}^{(x,y)}(i) &= \frac{4(\lambda/2)^2}{U} [S_{xz}^x S_{xy}^x - (S_{xz}^y S_{xy}^y + S_{xz}^z S_{xy}^z)] \\
&\quad + \frac{4(\lambda/2)^2}{U} [S_{xy}^y S_{yz}^y - (S_{xy}^x S_{yz}^x + S_{xy}^z S_{yz}^z)]
\end{aligned} \tag{7}$$

Neglecting the terms involving the S^z components which are suppressed by the easy-plane anisotropy discussed above, we obtain:

$$\begin{aligned}
[H_{\text{eff}}^{(2)}]_{\text{AD}}^{(x,y)}(i) &= -\frac{4(\lambda/2)^2}{U} [S_{xy}^x (S_{yz}^x - S_{xz}^x) + S_{xy}^y (S_{xz}^y - S_{yz}^y)] \\
&= -\frac{4(\lambda/2)^2}{U} f_{xy} S^2 [\sin 2\phi \sin \phi_c]
\end{aligned} \tag{8}$$

where the spin components are expressed as: $S_{xy}^x = f_{xy}S \cos \phi$, $S_{yz}^x = S \cos(\phi - \phi_c)$, $S_{xz}^x = S \cos(\phi + \phi_c)$ (and similarly for the y components) in terms of the overall orientation angle ϕ of the magnetic order and the relative canting angle $2\phi_c$ between the yz, xz moments. Here the factor $f_{xy} < 1$ represents the reduced moment for the xy orbital.

The above expression shows the composite orientation and canting angle dependence of the anisotropic interaction energy having the C_4 symmetry. Minimum energy is obtained at orientations $\phi = n\pi/4$ (where $n = 1, 3, 5, 7$) since the canting angle has the approximate functional form $\phi_c \approx \phi_c^{\max} \sin 2\phi$ in terms of the orientation ϕ . Thus, while the easy-plane anisotropy involves only the yz, xz moments, the xy moment plays a crucial role in the easy-axis anisotropy, which is directly relevant for NaOsO_3 (xy orbital is also nominally half-filled), but also for Ca_2RuO_4 with the factor f_{xy} as incorporated above.

For later reference, we note here that condensates of the orbital off-diagonal (OOD) one-body operators as in Eq. (4) directly yield physical quantities such as orbital magnetic moments and spin-orbital correlations:

$$\begin{aligned} \langle L_\alpha \rangle &= -i [\langle \psi_\mu^\dagger \psi_\nu \rangle - \langle \psi_\mu^\dagger \psi_\nu \rangle^*] = 2 \text{Im} \langle \psi_\mu^\dagger \psi_\nu \rangle \\ \langle L_\alpha S_\alpha \rangle &= -i [\langle \psi_\mu^\dagger \sigma_\alpha \psi_\nu \rangle - \langle \psi_\mu^\dagger \sigma_\alpha \psi_\nu \rangle^*] / 2 = \text{Im} \langle \psi_\mu^\dagger \sigma_\alpha \psi_\nu \rangle \\ \lambda_\alpha^{\text{int}} &= (U'' - J_H/2) \langle L_\alpha S_\alpha \rangle = (U'' - J_H/2) \text{Im} \langle \psi_\mu^\dagger \sigma_\alpha \psi_\nu \rangle \end{aligned} \quad (9)$$

where the orbital pair (μ, ν) corresponds to the component $\alpha = x, y, z$, and the last equation yields the interaction induced SOC renormalization, as discussed in the next section.

III. SELF-CONSISTENT DETERMINATION OF MAGNETIC ORDER

We consider the various contributions from the Coulomb interaction terms (Eq. 3) in the HF approximation, focussing first on terms with normal (orbital diagonal) spin and charge condensates. The resulting local spin and charge terms can be written as:

$$[\mathcal{H}_{\text{int}}^{\text{HF}}]_{\text{normal}} = \sum_{i\mu} \psi_{i\mu}^\dagger [-\boldsymbol{\sigma} \cdot \boldsymbol{\Delta}_{i\mu} + \mathcal{E}_{i\mu} \mathbf{1}] \psi_{i\mu} \quad (10)$$

where the spin and charge fields are self-consistently determined from:

$$\begin{aligned} 2\Delta_{i\mu}^\alpha &= U \langle \sigma_{i\mu}^\alpha \rangle + J_H \sum_{\nu < \mu} \langle \sigma_{i\nu}^\alpha \rangle \quad (\alpha = x, y, z) \\ \mathcal{E}_{i\mu} &= \frac{U \langle n_{i\mu} \rangle}{2} + U'' \sum_{\nu < \mu} \langle n_{i\nu} \rangle \end{aligned} \quad (11)$$

in terms of the local charge density $\langle n_{i\mu} \rangle$ and the spin density components $\langle \sigma_{i\mu}^\alpha \rangle$.

There are additional contributions resulting from orbital off-diagonal (OOD) spin and charge condensates which are finite due to orbital mixing induced by SOC and structural distortions (octahedral tilting and rotation). The contributions corresponding to different Coulomb interaction terms are summarized in Appendix A, and can be grouped in analogy with Eq. (10) as:

$$[\mathcal{H}_{\text{int}}^{\text{HF}}]_{\text{OOD}} = \sum_{i,\mu<\nu} \psi_{i\mu}^\dagger [-\boldsymbol{\sigma} \cdot \boldsymbol{\Delta}_{i\mu\nu} + \mathcal{E}_{i\mu\nu} \mathbf{1}] \psi_{i\nu} + \text{H.c.} \quad (12)$$

where the orbital off-diagonal spin and charge fields are self-consistently determined from:

$$\begin{aligned} \boldsymbol{\Delta}_{i\mu\nu} &= \left(\frac{U''}{2} + \frac{J_{\text{H}}}{4} \right) \langle \boldsymbol{\sigma}_{i\nu\mu} \rangle + \left(\frac{J_{\text{P}}}{2} \right) \langle \boldsymbol{\sigma}_{i\mu\nu} \rangle \\ \mathcal{E}_{i\mu\nu} &= \left(-\frac{U''}{2} + \frac{3J_{\text{H}}}{4} \right) \langle n_{i\nu\mu} \rangle + \left(\frac{J_{\text{P}}}{2} \right) \langle n_{i\mu\nu} \rangle \end{aligned} \quad (13)$$

in terms of the corresponding condensates $\langle \boldsymbol{\sigma}_{i\mu\nu} \rangle \equiv \langle \psi_{i\mu}^\dagger \boldsymbol{\sigma} \psi_{i\nu} \rangle$ and $\langle n_{i\mu\nu} \rangle \equiv \langle \psi_{i\mu}^\dagger \mathbf{1} \psi_{i\nu} \rangle$.

The spin and charge condensates in Eqs. 11 and 13 are evaluated using the eigenfunctions ($\phi_{\mathbf{k}}$) and eigenvalues ($E_{\mathbf{k}}$) of the full Hamiltonian in the given basis including the interaction contributions $[\mathcal{H}_{\text{int}}^{\text{HF}}]$ (Eqs. 10 and 12) using:

$$\langle \sigma_{i\mu\nu}^\alpha \rangle \equiv \langle \psi_{i\mu}^\dagger \sigma^\alpha \psi_{i\nu} \rangle = \sum_{\mathbf{k}}^{E_{\mathbf{k}} < E_{\text{F}}} (\phi_{\mathbf{k}\mu s \uparrow}^* \phi_{\mathbf{k}\mu s \downarrow}^*) [\sigma^\alpha] \begin{pmatrix} \phi_{\mathbf{k}\nu s \uparrow} \\ \phi_{\mathbf{k}\nu s \downarrow} \end{pmatrix} \quad (14)$$

for site i on the $s = A/B$ sublattice, and similarly for the charge condensates $\langle n_{i\mu\nu} \rangle \equiv \langle \psi_{i\mu}^\dagger \mathbf{1} \psi_{i\nu} \rangle$ with the Pauli matrices $[\sigma^\alpha]$ replaced by the unit matrix $[\mathbf{1}]$. The normal spin and charge condensates correspond to $\nu = \mu$. For each orbital pair $(\mu, \nu) = (yz, xz), (xz, xy), (xy, yz)$, there are three components ($\alpha = x, y, z$) for the spin condensates $\langle \psi_{i\mu}^\dagger \sigma_\alpha \psi_{i\nu} \rangle$ and one charge condensate $\langle \psi_{i\mu}^\dagger \mathbf{1} \psi_{i\nu} \rangle$. This is analogous to the three-plus-one normal spin and charge condensates for each of the three orbitals $\mu = yz, xz, xy$.

The above additional terms involving orbital off-diagonal condensates contribute to orbital physics. Thus, the charge terms lead to coupling of orbital angular momentum operators to weak orbital fields, the spin terms result in interaction-induced SOC renormalization as given in Eq. (9), and the self consistently determined renormalized SOC values are obtained as:

$$\lambda_\alpha = \lambda + \lambda_\alpha^{\text{int}} \quad (15)$$

for the three components $\alpha = x, y, z$. Results of the self consistent determination of magnetic order including all orbital diagonal and off-diagonal spin and charge condensates have been presented for the $4d^4$ compound Ca_2RuO_4 recently,⁵² illustrating the rich interplay between different physical elements.

IV. GENERALIZED FLUCTUATION PROPAGATOR

Since all generalized spin $\langle \psi_\mu^\dagger \boldsymbol{\sigma} \psi_\nu \rangle$ and charge $\langle \psi_\mu^\dagger \psi_\nu \rangle$ condensates were included in the self consistent determination of magnetic order, the fluctuation propagator must also be defined in terms of the generalized operators. We therefore consider the time-ordered generalized fluctuation propagator:

$$[\chi(\mathbf{q}, \omega)] = \int dt \sum_i e^{i\omega(t-t')} e^{-i\mathbf{q} \cdot (\mathbf{r}_i - \mathbf{r}_j)} \times \langle \Psi_0 | T[\sigma_{\mu\nu}^\alpha(i, t) \sigma_{\mu'\nu'}^{\alpha'}(j, t')] | \Psi_0 \rangle \quad (16)$$

in the self-consistent AFM ground state $|\Psi_0\rangle$, where the generalized spin-charge operators at lattice sites i, j are defined as $\sigma_{\mu\nu}^\alpha = \psi_\mu^\dagger \sigma^\alpha \psi_\nu$, which include both the orbital diagonal ($\mu = \nu$) and off-diagonal ($\mu \neq \nu$) cases, as well as the spin ($\alpha = x, y, z$) and charge ($\alpha = c$) operators, with σ^α defined as Pauli matrices for $\alpha = x, y, z$ and unit matrix for $\alpha = c$.

In the random phase approximation (RPA), the generalized fluctuation propagator is obtained as:

$$[\chi(\mathbf{q}, \omega)]_{\text{RPA}} = \frac{2[\chi^0(\mathbf{q}, \omega)]}{\mathbf{1} - [U][\chi^0(\mathbf{q}, \omega)]} \quad (17)$$

in terms of the bare particle-hole propagator $[\chi^0(\mathbf{q}, \omega)]$ which is evaluated by integrating out the electronic degrees of freedom:

$$[\chi^0(\mathbf{q}, \omega)]_{\mu\nu\alpha s}^{\mu'\nu'\alpha' s'} = \frac{1}{2} \sum_{\mathbf{k}} \left[\frac{\langle \mathbf{k} | \sigma_{\mu\nu}^\alpha | \mathbf{k} - \mathbf{q} \rangle_s \langle \mathbf{k} | \sigma_{\mu'\nu'}^{\alpha'} | \mathbf{k} - \mathbf{q} \rangle_{s'}^*}{E_{\mathbf{k}-\mathbf{q}}^\oplus - E_{\mathbf{k}}^\ominus + \omega - i\eta} + \frac{\langle \mathbf{k} | \sigma_{\mu\nu}^\alpha | \mathbf{k} - \mathbf{q} \rangle_s \langle \mathbf{k} | \sigma_{\mu'\nu'}^{\alpha'} | \mathbf{k} - \mathbf{q} \rangle_{s'}^*}{E_{\mathbf{k}}^\oplus - E_{\mathbf{k}-\mathbf{q}}^\ominus - \omega - i\eta} \right] \quad (18)$$

The matrix elements in the above expression are evaluated using the eigenvectors of the HF Hamiltonian in the self-consistent AFM state:

$$\langle \mathbf{k} | \sigma_{\mu\nu}^\alpha | \mathbf{k} - \mathbf{q} \rangle_s = (\phi_{\mathbf{k}\mu\uparrow s}^* \quad \phi_{\mathbf{k}\mu\downarrow s}^*) [\sigma^\alpha] \begin{pmatrix} \phi_{\mathbf{k}-\mathbf{q} \ \nu\uparrow s} \\ \phi_{\mathbf{k}-\mathbf{q} \ \nu\downarrow s} \end{pmatrix} \quad (19)$$

and the superscripts \oplus (\ominus) refer to particle (hole) states above (below) the Fermi energy. The subscripts s, s' indicate the two (A/B) sublattices. In the composite spin-charge-orbital-sublattice ($\mu\nu\alpha s$) basis, the $[\chi^0(\mathbf{q}, \omega)]$ matrix is of order 72×72 , and the form of the $[U]$ matrix in the RPA expression (Eq. 17) is given in Appendix B.

The spectral function of the excitations will be determined from:

$$A_{\mathbf{q}}(\omega) = \frac{1}{\pi} \text{Im} \text{Tr}[\chi(\mathbf{q}, \omega)]_{\text{RPA}} \quad (20)$$

using the RPA expression for $[\chi(\mathbf{q}, \omega)]$. When the collective excitation energies lie within the AFM band gap, it is convenient to consider the symmetric form of the denominator in the RPA expression (Eq. 17):

$$[U][\chi^0(\mathbf{q}, \omega)][U] - [U] \quad (21)$$

and in terms of the real eigenvalues $\lambda_{\mathbf{q}}(\omega)$ of this Hermitian matrix, the magnon energies $\omega_{\mathbf{q}}$ for momentum \mathbf{q} are determined by solving for the zeroes:

$$\lambda_{\mathbf{q}}(\omega = \omega_{\mathbf{q}}) = 0 \quad (22)$$

corresponding to the poles in the propagator.

Results of the calculated spectral function will be discussed in the subsequent sections for different electron filling cases ($n = 3, 4, 5$) with applications to corresponding $4d$ and $5d$ transition metal compounds. Broadly, our investigation of the generalized fluctuation propagator will provide information about the dominantly spin, orbital, and spin-orbital excitations, as the generalized spin and charge operators $\psi_{\mu}^{\dagger} \sigma^{\alpha} \psi_{\nu}$ include spin ($\mu = \nu$, $\alpha = x, y, z$), orbital ($\mu \neq \nu$, $\alpha = c$), and spin-orbital ($\mu \neq \nu$, $\alpha = x, y, z$) cases. Also included will be the high-energy spin-orbit exciton modes involving particle-hole excitations across the renormalized spin-orbit gap between spin-orbital entangled states of different J sectors, as in the $n = 5$ case relevant for the Sr_2IrO_4 compound.

V. $n = 3$ — APPLICATION TO NaOsO_3

The strongly spin-orbit coupled orthorhombic structured $5d^3$ osmium compound NaOsO_3 , with nominally three electrons in the Os t_{2g} sector, exhibits several novel electronic and magnetic properties. These include a G-type antiferromagnetic (AFM) structure with spins

oriented along the c axis, a significantly reduced magnetic moment $\sim 1\mu_B$ as measured from neutron scattering, a continuous metal-insulator transition (MIT) that coincides with the AFM transition ($T_N = T_{MIT} = 410$ K) as seen in neutron and X-ray scattering, and a large magnon gap of 58 meV as seen in resonant inelastic X-ray scattering (RIXS) measurements indicating strong magnetic anisotropy.^{8–10,16}

Two different mechanisms contributing to SOC-induced easy-plane anisotropy and large magnon gap for out-of-plane fluctuation modes were identified for the weakly correlated $5d^3$ compound NaOsO_3 in terms of a simplified picture involving only the normal spin and charge densities.^{14,15} Both essential ingredients — (i) small moment disparity between yz , xz and xy orbitals and (ii) spin-charge coupling effect in presence of tetragonal splitting — are intrinsically present in the considered three-orbital model on the square lattice. A realistic representation of magnetic anisotropy in NaOsO_3 is therefore provided by the considered model, while maintaining uniformity of lattice structure across the $n = 3, 4, 5$ cases considered in order to keep the focus on coupled spin-orbital fluctuations.

The first mechanism involves the SOC-induced anisotropic interaction terms as in Eq. (6) resulting from the three SOC terms $-\lambda L_\alpha S_\alpha$ for $\alpha = x, y, z$. Due to the small moment disparity $m_{yz,xz} > m_{xy}$ resulting from the broader xy band, the interaction term in Eq. (6) dominates over the other two terms, leading to the easy-plane anisotropy for parallel yz , xz moments enforced by the Hund's coupling. With increasing U , this effect weakens as the moments saturate $m_{yz,xz,xy} \approx 1$ in the large U limit. In the second mechanism, the SOC induced decreasing xy orbital density n_{xy} with spin rotation from z direction to $x - y$ plane couples to the tetragonal distortion term, and for positive ϵ_{xy} the energy is minimized for spin orientation in the $x - y$ plane.

We will consider the parameter set values $U = 4$, $J_H = U/5$, $U'' = U - 5J_H/2$, bare SOC value $\lambda=1.0$, and $\epsilon_{xy} = 0.5$ unless otherwise indicated, with the hopping energy scale $|t_1|=300$ meV. Thus, $U = 1.2$ eV, $\lambda=0.3$ eV, $\epsilon_{xy} = 0.15$ eV, which are realistic values for the NaOsO_3 compound. Initially, we will also set $t_{m1,m2,m3} = 0$ for simplicity, and focus on the easy-plane anisotropy and large magnon gap for out-of-plane fluctuations.

Self consistent determination of magnetic order using the generalized approach discussed in Sec. III confirms the easy-plane anisotropy. Starting in nearly z direction, the AFM order direction self consistently approaches the $x - y$ plane in a few hundred iterations. Initially, we will discuss magnetic excitations in the self consistent state with AFM order along the

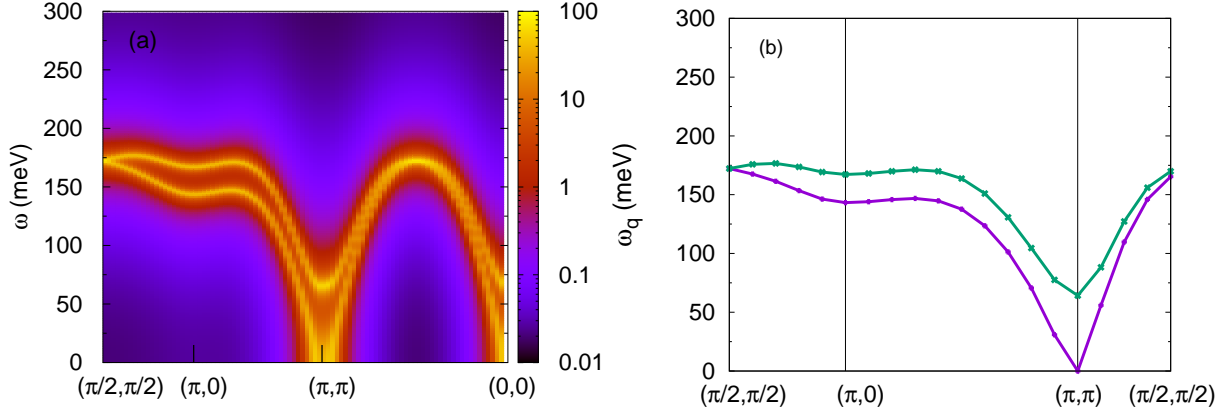


FIG. 2: (a) Low energy part of the calculated spectral function from the generalized fluctuation propagator shows the magnon excitations in the self-consistent state with planar AFM order, and (b) magnon dispersion showing the gapless and gapped modes corresponding to in-plane and out-of-plane fluctuations.

\hat{x} or \hat{y} directions. Although these orientations correspond to metastable states as discussed later, they provide convenient test cases for explicitly confirming the gapless in-plane and gapped out-of-plane magnon modes in the generalized fluctuation propagator calculation.

The low-energy part of the calculated spectral function using Eq. (20) is shown in the Fig. 2(a) as an intensity plot for \mathbf{q} along symmetry directions of the Brillouin zone. The gapless and gapped modes corresponding to in-plane and out-of-plane fluctuations reflect the easy-plane magnetic anisotropy. The calculated gap energy 60 meV is close to the measured spin wave gap of 58 meV in NaOsO_3 . Also shown for comparison in Fig. 2(b) is the magnon dispersion calculated from the poles of the RPA propagator as described in Sec. IV. Focussing on the magnon gap in Fig. 2(b), which provides a measure of the SOC induced easy-plane anisotropy, effects of various physical quantities are shown in Fig. 3.

The gapless Goldstone mode corresponding to in-plane rotation of AFM ordering direction in the $x - y$ plane involves only small changes in spin densities $\langle \psi_\mu^\dagger \sigma^\alpha \psi_\mu \rangle$ for $\alpha = x, y$ and $\mu = yz, xz$, and also in generalized spin densities $\langle \psi_\mu^\dagger \sigma^\alpha \psi_\nu \rangle$ for $\alpha = x, y$ and $\mu = yz, xz$ with fixed $\nu = xy$. For example, the magnetization values $m_{yz}^x = 0.82$ and $m_{xz}^x = 0.84$ change to $m_{yz}^y = 0.84$ and $m_{xz}^y = 0.82$ when the ordering is rotated from x to y direction. Thus, the Goldstone mode is nearly pure spin mode and the small orbital character reflects the effectively suppressed spin-orbital entanglement in the $n = 3$ AFM state. In contrast, the

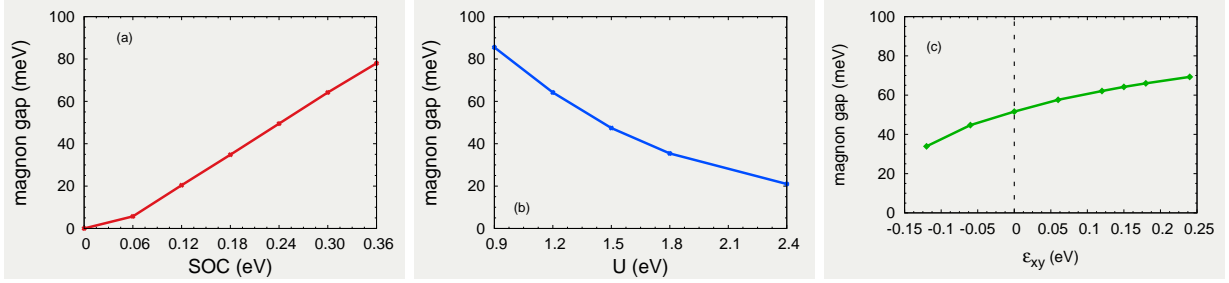


FIG. 3: Variation of the calculated magnon gap showing effects of (a) SOC, (b) Hubbard U , and (c) tetragonal distortion ϵ_{xy} , on the easy-plane magnetic anisotropy.

$n = 5$ case corresponding to Sr_2IrO_4 shows strongly coupled spin-orbital character of the Goldstone mode (Appendix C) due to the extreme spin-orbital entanglement.

We now consider the easy-axis anisotropy effects in our self consistent determination of magnetic order. With respect to the AFM order orientation (azimuthal angle ϕ) within the easy ($x-y$) plane, we find an easy-axis anisotropy along the diagonal orientations $\phi = n\pi/4$ ($n = 1, 3, 5, 7$) even for no octahedral tilting. This anisotropy is due to the orientation and canting angle dependent anisotropic interaction (Eq. 8) as discussed in Sec. II. The anisotropic interaction energy vanishes for ϕ along the x, y axes (hence the gapless in-plane mode in Fig. 2), and is significant near the diagonal orientations, resulting in easy-axis anisotropy and small relative canting between yz, xz moments which is explicitly confirmed in our self-consistent calculation.

The resulting C_4 symmetry of the easy-axis $\pm(\hat{x} \pm \hat{y})$ is reduced to C_2 symmetry $\pm(\hat{x} - \hat{y})$ in the presence of octahedral tilting. The important anisotropy effects of the octahedral tilting induced inter-site DM interactions are discussed below. We find that the DM axis lies along the crystal b axis, leading to easy axis direction along the crystal a axis. Both these directions are interchanged in comparison to the Ca_2RuO_4 case, which follows from a subtle difference in the present $n = 3$ case as explained below.

Following the analysis carried out for the Ca_2RuO_4 compound,⁵² within the usual strong-coupling expansion in terms of the normal (t) and spin-dependent (t'_x, t'_y) hopping terms induced by the combination of SOC and orbital mixing hopping terms $t_{m2,m3}$ due to octahedral tilting, the DM interaction terms generated in the effective spin model are obtained

TABLE I: Self consistently determined magnetization and density values for the three orbitals (μ) on the two sublattices (s), showing easy-axis anisotropy along the crystal a axis due to octahedral tilting induced DM interaction. Here $t_{m2,m3} = 0.15$.

μ (s)	m_μ^x	m_μ^y	m_μ^z	n_μ	μ (s)	m_μ^x	m_μ^y	m_μ^z	n_μ
yz (A)	0.598	-0.557	0.006	1.012	yz (B)	-0.598	0.557	0.006	1.012
xz (A)	0.557	-0.598	-0.006	1.012	xz (B)	-0.557	0.598	-0.006	1.012
xy (A)	0.541	-0.541	0.0	0.977	xy (B)	-0.541	0.541	0.0	0.977

TABLE II: Self consistently determined renormalized SOC values $\lambda_\alpha = \lambda + \lambda_\alpha^{\text{int}}$ and the orbital magnetic moments $\langle L_\alpha \rangle$ for $\alpha = x, y, z$ on the two sublattices. Bare SOC value $\lambda=1.0$.

s	λ_x	λ_y	λ_z	$\langle L_x \rangle$	$\langle L_y \rangle$	$\langle L_z \rangle$
A	1.179	1.179	1.364	0.032	-0.032	0.0
B	1.179	1.179	1.364	-0.032	0.032	0.0

as:

$$\begin{aligned}
[H_{\text{eff}}^{(2)}]_{\text{DM}}^{(x,y)} &= \frac{8tt'_x}{U} \sum_{\langle i,j \rangle_x} \hat{x} \cdot (\mathbf{S}_{i,xz} \times \mathbf{S}_{j,xz}) + \frac{8tt'_y}{U} \sum_{\langle i,j \rangle_y} \hat{y} \cdot (\mathbf{S}_{i,yz} \times \mathbf{S}_{j,yz}) \\
&\approx \frac{8t|t'_x|}{U} \sum_{\langle i,j \rangle} (\hat{x} + \hat{y}) \cdot (\mathbf{S}_{i,yz} \times \mathbf{S}_{j,yz})
\end{aligned} \tag{23}$$

where we have taken $t'_x = -t'_y = -\text{ive}$ and $S_{i,xz}^x = S_{i,yz}^x$ (due to Hund's coupling) as earlier, but with $S_{i,xz}^z = -S_{i,yz}^z$ for the $n = 3$ case as obtained in our self consistent calculation which is discussed below. The effective DM axis $(\hat{x} + \hat{y})$ is thus along the crystal b axis (Fig. 1) for the yz orbital, resulting in easy-axis anisotropy along the crystal a direction, as well as spin canting about the DM axis in the z direction.

Results for various physical quantities are shown in Tables I and II. Starting with initial orientation along the \hat{x} or \hat{y} directions, the AFM order direction self consistently approaches the easy-axis direction in a few hundred iterations, explicitly exhibiting the strong easy-axis anisotropy within the easy ($x-y$) plane due to the octahedral tilting induced DM interaction,

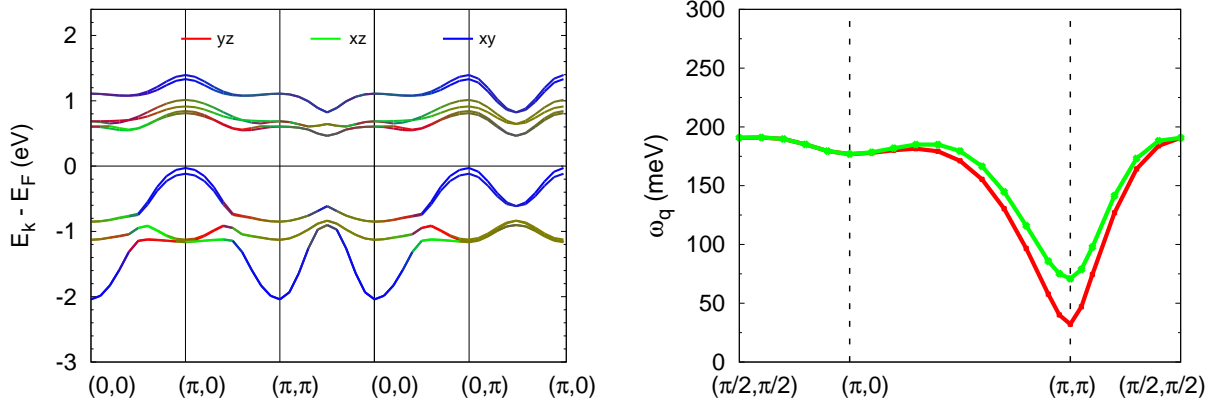


FIG. 4: (a) Calculated orbital resolved electronic band structure in the self-consistent state with AFM order along the crystal a axis due to octahedral tilting induced DM interaction. Here $t_{m2,m3} = 0.15$. Colors indicate dominant orbital weight: red (yz), green (xz), blue (xy). (b) Magnon dispersion for the magnetic order as given in Table I, showing that both in-plane and out-of-plane modes are appreciably gapped due to the easy-axis and easy-plane anisotropies.

along with small spin canting in the z direction about the DM axis. The small moment disparity $m_{yz,xz} > m_{xy}$ and the negligible orbital moments can also be seen here explicitly. The renormalized SOC strength λ_z is enhanced relative to the other two components, which further reduces the SOC induced frustration in this system with nominally one electron in each of the three orbitals.

With octahedral tilting included, the orbital resolved electronic band structure in the self-consistent AFM state (Fig. 4(a)) shows the AFM band gap between valence and conduction bands, SOC induced orbital mixing and band splittings, the fine splitting due to octahedral tilting, and the asymmetric bandwidth for xy orbital bands characteristic of the 2nd neighbor hopping term t_2 which connects the same magnetic sublattice. The calculated magnon dispersion evaluated using Eq. 22 is shown in Fig. 4(b). As expected, both in-plane and out-of-plane magnon modes are gapped due to the easy-axis and easy-plane anisotropies discussed above.

The high energy part of the spectral function is shown in the series of panels in Fig. 5 for different SOC strengths. The two groups of modes here correspond to: (i) the Hund's coupling induced gapped magnon modes for out-of-phase spin fluctuations (the two dispersive modes starting at energies 0.7 and 0.8 eV from the left edge in panel (a)), and (ii)

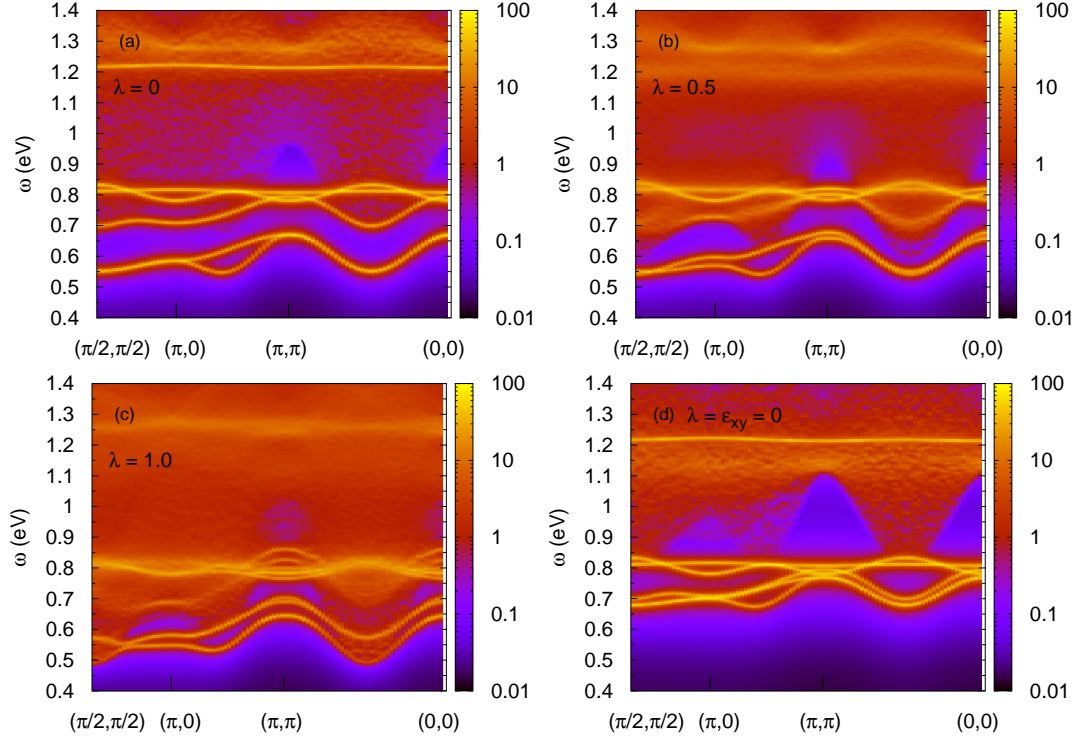


FIG. 5: Gapped magnon modes and dominantly magnetic exciton modes for the $n = 3$ case seen in the high-energy part of the spectral function calculated in the self consistent AFM state including octahedral tilting, for different SOC (λ) values shown in the panels.

the spin-orbiton modes (starting at energy below 0.6 eV) which are inter-orbital magnetic excitons corresponding to the lowest-energy particle-hole excitations across the AFM band gap involving yz/xz orbitals (particle) and xy orbital (hole) states (Fig. 4(a)). Through the usual resonant scattering mechanism, these modes are pulled down in energy below the continuum by the U'' interaction term, and form well defined propagating modes.

The spin-orbiton mode involving xy orbital shifts to higher energy when ϵ_{xy} decreases to zero (panel (d)) which lowers the dominantly xy valence band (Fig. 4(a)) and thus increases the particle-hole excitation energy. The splitting of the exciton modes in panel (c) is due to the SOC induced splitting of electronic bands as seen in Fig. 4(a), which is then reflected in the particle-hole excitation energies. The combination of orbitals for these exciton modes indicates that L_x and L_y components of the orbital angular momentum are involved in these coupled spin-orbital fluctuations. There is an additional spin-orbiton mode involving only yz, xz orbitals (and L_z component) which is formed at higher energy near 0.8 eV (flat band near the left edge in panel (a)). With increasing SOC, the high-energy modes involving

yz, xz orbitals acquire significant spin-orbit exciton character.

VI. $n = 5$ — APPLICATION TO Sr_2IrO_4

The perovskite structured $5d^5$ compound Sr_2IrO_4 exhibits an AFM insulating state due to strong SOC induced splitting of the t_{2g} states, with four electrons in the nominally filled and non-magnetic $J=3/2$ sector and one electron in the nominally half filled and magnetically active $J=1/2$ sector. The SOC induced splitting of $3\lambda/2$ between states of the two total angular momentum sectors, strong spin-orbital entanglement, and band narrowing of states in the $J=1/2$ sector, all of these play a crucial role in the stabilization of the AFM insulator state. Both low-energy magnon excitations and high-energy spin-orbit excitons across the renormalized spin-orbit gap have been intensively studied using RIXS experiments and variety of theoretical approaches.^{43,46,47,51,53}

In this case, we have taken realistic parameter values $U = 3$, $J_H = U/7$, bare SOC value $\lambda = 1.35$, and $\epsilon_{xy} = -0.5$ for simplicity, along with hopping terms: $(t_1, t_2, t_3, t_4, t_5, t_{m1}) = (-1.0, 0.5, 0.25, -1.0, 0.0, 0.2)$, all in units of the realistic hopping energy scale $|t_1|=290$ meV. The self consistently determined results for various physical quantities are given in Table III for magnetic order in the x direction. All ordering directions within the $x-y$ plane are nearly equivalent. Besides the dominant Hund's coupling induced easy-plane anisotropy,⁵³ there is an extremely weak easy-axis anisotropy which will be discussed at the end of this section. The octahedral rotation induces small in-plane canting of spins but the canting axis is free to orient in any direction. The strong Coulomb interaction induced SOC renormalization by nearly $2/3$ (Table IV) agrees with the pseudo-orbital based approach.⁵¹

TABLE III: Self consistently determined magnetization and density values, showing small spin canting about the z axis due to octahedral rotation induced DM interaction. Here $t_{m1} = 0.2$.

μ (s)	m_μ^x	m_μ^y	m_μ^z	n_μ	μ (s)	m_μ^x	m_μ^y	m_μ^z	n_μ
yz (A)	0.186	-0.052	0	1.653	yz (B)	-0.186	-0.052	0	1.653
xz (A)	-0.185	0.049	0	1.654	xz (B)	0.185	0.049	0	1.654
xy (A)	-0.172	-0.047	0	1.693	xy (B)	0.172	-0.047	0	1.693

TABLE IV: Self consistently determined renormalized SOC values $\lambda_\alpha = \lambda + \lambda_\alpha^{\text{int}}$ and the orbital magnetic moments $\langle L_\alpha \rangle$ for $\alpha = x, y, z$ on the two sublattices. Bare SOC value $\lambda=1.35$.

s	λ_x	λ_y	λ_z	$\langle L_x \rangle$	$\langle L_y \rangle$	$\langle L_z \rangle$
A	1.882	1.882	1.871	0.367	0.091	0
B	1.882	1.882	1.871	-0.367	0.091	0

The strong orbital moments and their correlation with the magnetic order direction (Table IV) reflect the strong SOC induced spin-orbital entanglement.

The low energy part of the spectral function (Fig. 6(a)) clearly shows the gapless and gapped modes corresponding to in-plane and out-of-plane fluctuations, consistent with the easy-plane anisotropy. The magnon gap ≈ 45 meV is close to the result obtained using the pseudo-orbital based approach,⁵³ and in agreement with recent experiments.⁴⁶ It should be noted that along with the full generalized spin sector, the orbital off-diagonal charge sector ($\psi_\mu^\dagger \mathbf{1} \psi_\nu$) related to the orbital moment operators $L_{x,y,z}$ was included in the above calculations which allows for the accompanying transverse fluctuations of orbital moments. Indeed, the exactly gapless Goldstone mode seen in Fig. 6(a) is obtained only if the $\psi_\mu^\dagger \mathbf{1} \psi_\nu$ sector is included, indicating the coupled spin-orbital nature of the Goldstone mode, as illustrated in

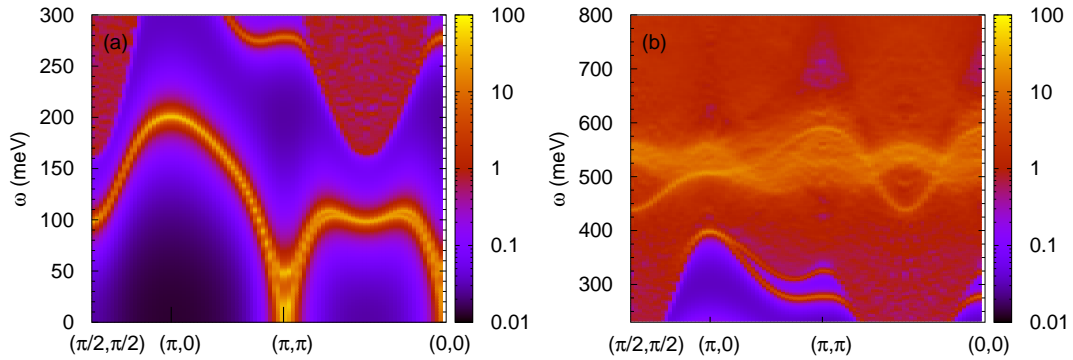


FIG. 6: The spectral function in the self-consistent state for the $n = 5$ case with planar AFM order including octahedral rotation, showing the (a) gapless and gapped modes corresponding to in-plane and out-of-plane fluctuations and (b) the spin-orbit exciton modes near 500 meV and 300 meV in the high-energy part.

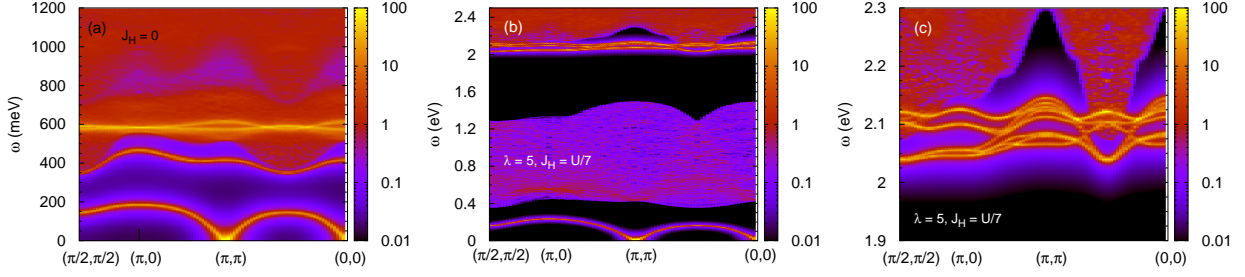


FIG. 7: The spin-orbit exciton modes ($n = 5$) for special cases showing (a) no splitting in the weak branch (~ 400 meV) for Hund's coupling $J_H = 0$, (b) disappearance of the weak branch for large SOC value $\lambda = 5$, and (c) expanded view of the multiple exciton modes (~ 2 eV) in case (b). Here octahedral rotation is included in all three cases.

Appendix C showing the detailed spin-orbital composition.

Fig. 6(b) shows the spin-orbit exciton modes (~ 500 meV) involving particle-hole excitations between the $J=1/2$ and $3/2$ sectors, which matches closely with results obtained using the pseudo-orbital based approach.⁵¹ As discussed in the previous ($n = 3$) case, collective modes arise from particle-hole excitations which are converted to well defined propagating modes split off from the continuum by the Coulomb interaction induced resonant scattering mechanism. The significantly weaker modes (~ 300 meV) just below the particle-hole continuum for the nominally $J = 1/2$ sector are also spin-orbit exciton modes. The splitting seen beyond $(\pi, 0)$ vanishes for $J_H = 0$, as seen in Fig. 7(a). The weak intensity corresponds to the small $J = 3/2$ character (mainly $m_J = \pm 3/2$) in the nominally $J = 1/2$ bands due to strong mixing between the two sectors induced by the band (hopping) terms. For large SOC strength λ , the weak exciton modes disappear (Fig. 7(b)), confirming the above picture. Thus, the (low) intensity of the weak exciton modes provides a direct measure of the mixing between the $J = 1/2$ and $3/2$ sectors. The fine splitting of exciton bands in Fig. 7(c) corresponds to four possible m_J values ($\pm 3/2, \pm 1/2$) for the hole in the $J = 3/2$ sector and the exciton hopping terms connecting the two sublattices.

We now discuss the extremely weak easy-axis anisotropy which leads to preferred isospin ($J = 1/2$) orientation along the diagonal directions $\pm(\hat{x} \pm \hat{y})$ within the easy plane. Fig. 8(a) shows the small magnon gap (≈ 3 meV) for the in-plane magnon mode induced by the Hund's coupling J_H due to the extremely weak spin twisting as shown in Fig. 8(b) which results in an easy-axis anisotropy with C_4 symmetry. Here the parameter set is same as

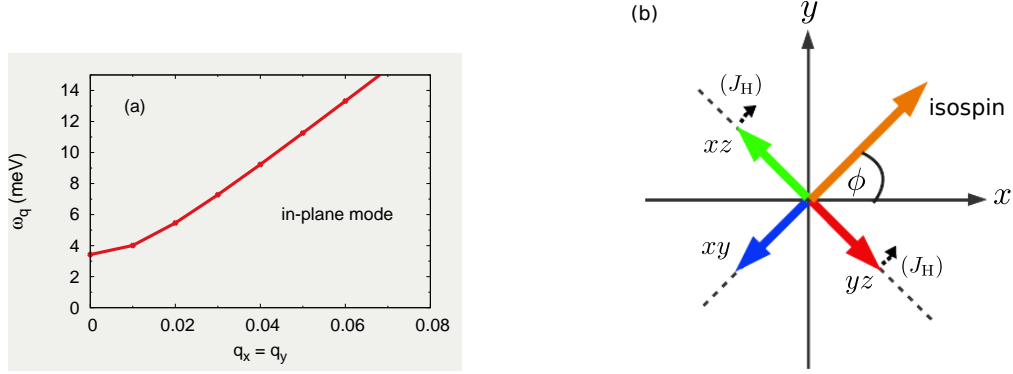


FIG. 8: (a) Magnon energies for isospin order along $\hat{x} + \hat{y}$ direction showing the small magnon gap (≈ 3 meV) for the in-plane fluctuation mode. (b) The isospin and yz, xz, xy moment orientations for the ideal spin-orbital entangled state, which is extremely weakly perturbed by finite J_H resulting in slight twisting of the yz, xz moments as indicated, leading to the easy-axis anisotropy with C_4 symmetry. The isospin easy axes are along $\phi = n\pi/4$ where $n = 1, 3, 5, 7$.

earlier including the octahedral rotation which only weakly enhances the magnon gap. The above weak perturbative effect of J_H on the strongly spin-orbital entangled state corresponds to the opposite end of the competition between SOC and J_H as compared to the $n = 3$ case discussed in Sec. V.

VII. $n = 4$ — APPLICATION TO Ca_2RuO_4

For moderate tetragonal distortion ($\epsilon_{xy} \approx -1$), the xy orbital in the $4d^4$ compound Ca_2RuO_4 is nominally doubly occupied and magnetically inactive, while the nominally half-filled and magnetically active yz, xz orbitals yield an effectively two-orbital magnetic system. Hund's coupling between the two $S = 1/2$ spins results in low-lying (in-phase) and appreciably gapped (out-of-phase) spin fluctuation modes. The in-phase modes of the yz, xz orbital $S = 1/2$ spins correspond to an effective $S = 1$ spin system. However, the rich interplay between SOC, Coulomb interaction, octahedral rotations, and tetragonal distortion results in complex magnetic behaviour which crucially involves the xy orbital and is therefore beyond the above simplistic picture.

Treating all the different physical elements on the same footing within the unified framework of the generalized self-consistent approach explicitly shows the variety of physical

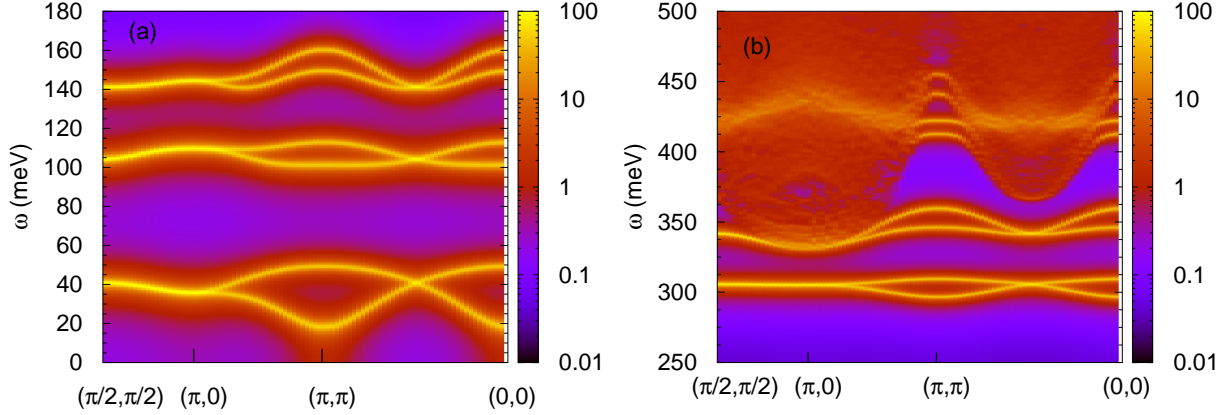


FIG. 9: The generalized fluctuation spectral function for the $n = 4$ case, showing coupled spin-orbital excitations including low-energy magnon modes (below ~ 60 meV), intermediate-energy orbiton (100 and 140 meV) and spin-orbiton (300 and 350 meV) modes, and high-energy spin-orbit exciton (425 meV) modes.

effects arising from the rich interplay in Ca_2RuO_4 . These include: SOC induced easy-plane and easy-axis anisotropies similar to the $n=3$ case, octahedral tilting induced reduction of easy-axis anisotropy from C_4 to C_2 symmetry, spin-orbital coupling induced orbital magnetic moments, Coulomb interaction induced strongly anisotropic SOC renormalization, decreasing tetragonal distortion induced magnetic reorientation transition from planar AFM order to FM (z) order, and orbital moment interaction induced orbital gap.⁵² Stable FM and AFM metallic states were also obtained near the magnetic phase boundary separating the two magnetic orders. The self-consistent determination of magnetic order has also explicitly shown the coupled nature of spin and orbital fluctuations, as reflected in the ferro and antiferro orbital fluctuations associated with in-phase and out-of-phase spin twisting modes, highlighting the strong deviation from conventional Heisenberg behaviour in effective spin models, as discussed recently to account for the magnetic excitation measurements in INS experiments on Ca_2RuO_4 .³⁵

In the following, we will take the same parameter set as considered in the self-consistent study,⁵² along with $U = 8$ and $J_H = U/5$ in the energy scale unit (150 meV), so that $U = 1.2$ eV, $U'' = U/2 = 0.6$ eV, and $J_H = 0.24$ eV. These are comparable to reported values extracted from RIXS ($J_H = 0.34$ eV) and ARPES ($J_H = 0.4$ eV) studies.^{24,40} The hopping parameter values considered are as given in Sec. II, and the bare SOC value $\lambda = 1$.

Fig. 9 shows the calculated generalized fluctuation spectral function. Several well defined propagating modes are seen here including: (i) the low-energy (below ~ 60 meV) dominantly spin (magnon) excitations involving the magnetically active yz, xz orbitals and corresponding to in-plane and out-of-plane fluctuations which are gapped due to the magnetic anisotropies, (ii) the intermediate-energy (100 and 140 meV) dominantly orbital excitations (orbitons) involving particle-hole excitations between xy (hole) and yz, xz (particle) states, (iii) the intermediate-energy (300 and 350 meV) dominantly spin-orbital excitations (spin-orbitons) involving xy (hole) and yz, xz (particle) states, and (iv) the high-energy (425 meV) dominantly spin-orbital excitations (spin-orbit excitons) involving particle-hole excitations between yz, xz (hole) and yz, xz (particle) states of nominally different J sectors. The SOC-induced spin-orbital entangled J states are strongly renormalized by the tetragonal splitting and the electronic correlation induced staggered field.

The spin-orbital characterization of the various collective excitations mentioned above is inferred from the basis-resolved contributions to the total spectral functions which explicitly show the relative spin-orbital composition of the various excitations (Appendix C). The presence of sharply defined collective excitations for the magnon, orbion, and spin-orbion modes which are clearly separated from the particle-hole continuum highlights the rich spin-orbital physics in the $n = 4$ case corresponding to the Ca_2RuO_4 compound. Many of our calculated magnon spectra features such as the magnon gaps for in-plane and out-of-plane modes, weak dispersive nature along the magnetic zone boundary, as well as the overall magnon energy scale are in excellent agreement with the INS study.^{34,35} The orbion mode energy scale is also qualitatively comparable to the composite excitation peaks obtained around 80 meV in Raman and RIXS studies.³⁷⁻⁴⁰ The calculated spin-orbion and spin-orbit exciton energies are also in agreement with the excitation peaks obtained around 300-350 meV energy range and 400 meV in RIXS studies. We also obtained excitations in the high-energy range 750-800 meV and 900 meV (not shown), which are comparable to the peaks obtained around 750 meV and 1000 meV in RIXS studies.

VIII. CONCLUSIONS

Following up on the generalized self-consistent approach including orbital off-diagonal spin and charge condensates, investigation of the generalized fluctuation propagator reveals the composite spin-orbital character of the different types of collective excitations in strongly spin-orbit coupled systems. A realistic representation of magnetic anisotropy effects due to the interplay of SOC, Coulomb interaction, and structural distortion terms was included in the three-orbital model, while maintaining uniformity of lattice structure in order to focus on the coupled spin-orbital excitations. Our unified investigation of the three electron filling cases $n = 3, 4, 5$ corresponding to the three compounds NaOsO_3 , Ca_2RuO_4 , Sr_2IrO_4 provides deep insight into how the spin-orbital physics in the magnetic ground state is reflected in the collective excitations. The calculated spectral functions show well defined propagating modes corresponding to dominantly spin (magnon), orbital (orbiton), and spin-orbital (spin-orbiton) excitations, along with the spin-orbit exciton modes involving spin-orbital excitations between states of different J sectors induced by the spin-orbit coupling.

Appendix A: Orbital off-diagonal condensates in the HF approximation

The additional contributions in the HF approximation arising from the orbital off-diagonal spin and charge condensates are given below. For the density, Hund's coupling, and pair hopping interaction terms in Eq. 3, we obtain (for site i):

$$\begin{aligned}
U'' \sum_{\mu < \nu} n_{\mu} n_{\nu} &\rightarrow -\frac{U''}{2} \sum_{\mu < \nu} [n_{\mu\nu} \langle n_{\nu\mu} \rangle + \boldsymbol{\sigma}_{\mu\nu} \cdot \langle \boldsymbol{\sigma}_{\nu\mu} \rangle] + \text{H.c.} \\
-2J_{\text{H}} \sum_{\mu < \nu} \mathbf{S}_{\mu} \cdot \mathbf{S}_{\nu} &\rightarrow \frac{J_{\text{H}}}{4} \sum_{\mu < \nu} [3n_{\mu\nu} \langle n_{\nu\mu} \rangle - \boldsymbol{\sigma}_{\mu\nu} \cdot \langle \boldsymbol{\sigma}_{\nu\mu} \rangle] + \text{H.c.} \\
J_{\text{P}} \sum_{\mu \neq \nu} a_{\mu\uparrow}^{\dagger} a_{\mu\downarrow}^{\dagger} a_{\nu\downarrow} a_{\nu\uparrow} &\rightarrow \frac{J_{\text{P}}}{2} \sum_{\mu < \nu} [n_{\mu\nu} \langle n_{\mu\nu} \rangle - \boldsymbol{\sigma}_{\mu\nu} \cdot \langle \boldsymbol{\sigma}_{\mu\nu} \rangle] + \text{H.c.}
\end{aligned} \tag{A1}$$

in terms of the orbital off-diagonal spin ($\boldsymbol{\sigma}_{\mu\nu} = \psi_{\mu}^{\dagger} \boldsymbol{\sigma} \psi_{\nu}$) and charge ($n_{\mu\nu} = \psi_{\mu}^{\dagger} \mathbf{1} \psi_{\nu}$) operators. The orbital off-diagonal condensates are finite due to the SOC-induced spin-orbital correlations. These additional terms in the HF theory explicitly preserve the $\text{SU}(2)$ spin rotation symmetry of the various Coulomb interaction terms.

Collecting all the spin and charge terms together, we obtain the orbital off-diagonal

(OOD) contributions of the Coulomb interaction terms:

$$[\mathcal{H}_{\text{int}}^{\text{HF}}]_{\text{OOD}} = \sum_{\mu < \nu} \left[\left(-\frac{U''}{2} + \frac{3J_{\text{H}}}{4} \right) n_{\mu\nu} \langle n_{\nu\mu} \rangle + \left(\frac{J_{\text{P}}}{2} \right) n_{\mu\nu} \langle n_{\mu\nu} \rangle - \left(\frac{U''}{2} + \frac{J_{\text{H}}}{4} \right) \boldsymbol{\sigma}_{\mu\nu} \cdot \langle \boldsymbol{\sigma}_{\nu\mu} \rangle - \left(\frac{J_{\text{P}}}{2} \right) \boldsymbol{\sigma}_{\mu\nu} \cdot \langle \boldsymbol{\sigma}_{\mu\nu} \rangle \right] + \text{H.c.} \quad (\text{A2})$$

Appendix B: Coulomb interaction matrix elements in the orbital-pair basis

Corresponding to the above HF contributions in the orbital off-diagonal sector, we express the Coulomb interactions in terms of the generalized spin and charge operators (for site i):

$$[\mathcal{H}_{\text{int}}]_{\text{OOD}} = \sum_{\mu < \nu} \left[\left(-\frac{U''}{2} + \frac{3J_{\text{H}}}{4} \right) n_{\mu\nu} n_{\mu\nu}^{\dagger} - \left(\frac{U''}{2} + \frac{J_{\text{H}}}{4} \right) \boldsymbol{\sigma}_{\mu\nu} \cdot \boldsymbol{\sigma}_{\mu\nu}^{\dagger} \right] + \sum_{\mu < \nu} \left[\left(\frac{J_{\text{P}}}{4} \right) n_{\mu\nu} n_{\nu\mu}^{\dagger} - \left(\frac{J_{\text{P}}}{4} \right) \boldsymbol{\sigma}_{\mu\nu} \cdot \boldsymbol{\sigma}_{\nu\mu}^{\dagger} + \text{H.c.} \right] \quad (\text{B1})$$

where $n_{\mu\nu}^{\dagger} = n_{\nu\mu}$ and $\boldsymbol{\sigma}_{\mu\nu}^{\dagger} = \boldsymbol{\sigma}_{\nu\mu}$. The above form shows that only the pair-hopping interaction terms (J_{P}) are off-diagonal in the orbital-pair ($\mu\nu$) basis. We will use the above Coulomb interaction terms in the orbital off-diagonal sector in the RPA series in order to ensure consistency with the self-consistent determination of magnetic order including the orbital off-diagonal condensates.

The Coulomb interaction terms in the orbital diagonal sector can be cast in a similar form:

$$[\mathcal{H}_{\text{int}}]_{\text{OD}} = \sum_{\mu} \left[\left(-\frac{U}{4} \right) \boldsymbol{\sigma}_{\mu} \cdot \boldsymbol{\sigma}_{\mu} + \left(\frac{U}{4} \right) n_{\mu} n_{\mu} \right] + \sum_{\mu < \nu} \left[\left(-\frac{2J_{\text{H}}}{4} \right) \boldsymbol{\sigma}_{\mu} \cdot \boldsymbol{\sigma}_{\nu} + U'' n_{\mu} n_{\nu} \right] \quad (\text{B2})$$

which include the Hubbard, Hund's coupling, and density interaction terms.

The form of the $[U]$ matrix used in the RPA series Eq. (17) is now discussed below. In the composite spin-charge-orbital-sublattice ($\mu\nu\alpha s$) basis, the $[U]$ matrix is diagonal in spin, charge, and sublattice sectors. There are two possible cases involving the orbital-pair ($\mu\nu$) basis. In the case $\mu = \nu$, the $[U]$ matrices in the spin ($\alpha = x, y, z$) and charge ($\alpha = c$) sectors are obtained as:

$$[U]_{\mu\mu\alpha=x,y,z}^{\mu'\mu'\alpha'=\alpha} = \begin{bmatrix} U & J_{\text{H}} & J_{\text{H}} \\ J_{\text{H}} & U & J_{\text{H}} \\ J_{\text{H}} & J_{\text{H}} & U \end{bmatrix} \quad [U]_{\mu\mu\alpha=c}^{\mu'\mu'\alpha'=\alpha} = \begin{bmatrix} -U & -2U'' & -2U'' \\ -2U'' & -U & -2U'' \\ -2U'' & -2U'' & -U \end{bmatrix} \quad (\text{B3})$$

FIG. 10: The basis-resolved contributions to the total spectral function for the low-energy magnon (left panel) and intermediate-energy orbiton (center and right panels) modes, showing dominantly spin ($\mu = \nu$, $\alpha = x, y, z$) and orbital ($\mu \neq \nu$, $\alpha = c$) character of the fluctuation modes, respectively.

$$\begin{aligned} [U]_{\mu\nu\alpha=x,y,z}^{\mu\nu\alpha} &= U'' + J_{\text{H}}/2 & [U]_{\mu\nu\alpha=c}^{\mu\nu\alpha} &= U'' - 3J_{\text{H}}/2 \\ [U]_{\mu\nu\alpha=x,y,z}^{\nu\mu\alpha} &= J_{\text{P}} & [U]_{\mu\nu\alpha=c}^{\nu\mu\alpha} &= -J_{\text{P}} \end{aligned} \quad (\text{B4})$$

Appendix C: Basis-resolved contributions to the total spectral function

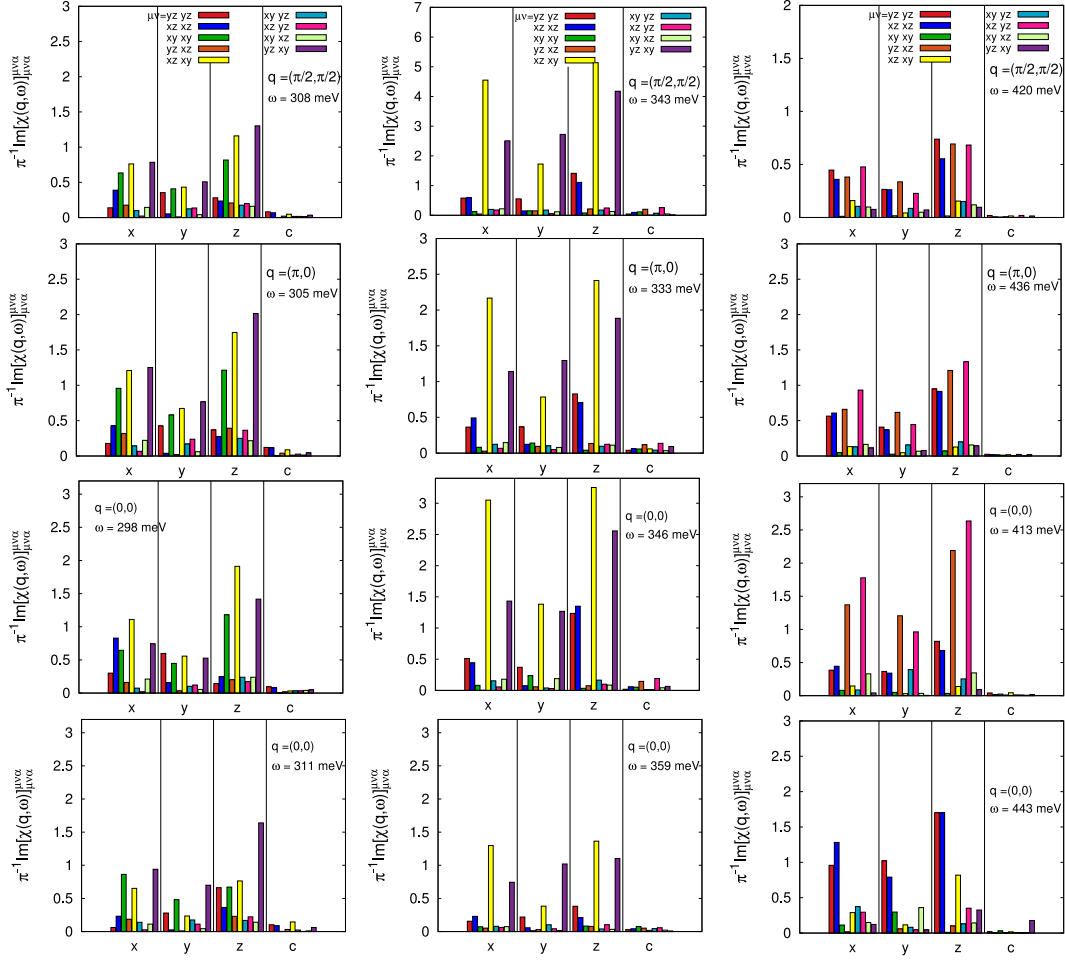


FIG. 11: The basis-resolved contributions to the total spectral function for the intermediate-energy spin-orbiton (left and center panels) and high-energy spin-orbit exciton (right panel) modes, showing dominantly spin-orbital character ($\mu \neq \nu$, $\alpha = x, y, z$) involving xy and yz, xz orbitals (left and center panels) and yz, xz orbitals (right panel).

excitations shown in Fig. 9 for the $n = 4$ case corresponding to the Ca_2RuO_4 compound. Fig. 10 shows dominantly spin excitations involving yz, xz orbitals for the magnon modes (below 60 meV) and dominantly orbital excitations involving xy and yz, xz orbitals for the orbiton modes (100 and 140 meV). Similarly, Fig. 11 shows dominantly spin-orbital excitations involving xy and yz, xz orbitals for the spin-orbiton modes (300 and 350 meV), and dominantly spin-orbital excitations involving yz, xz orbitals for the spin-orbit exciton modes (425 meV).

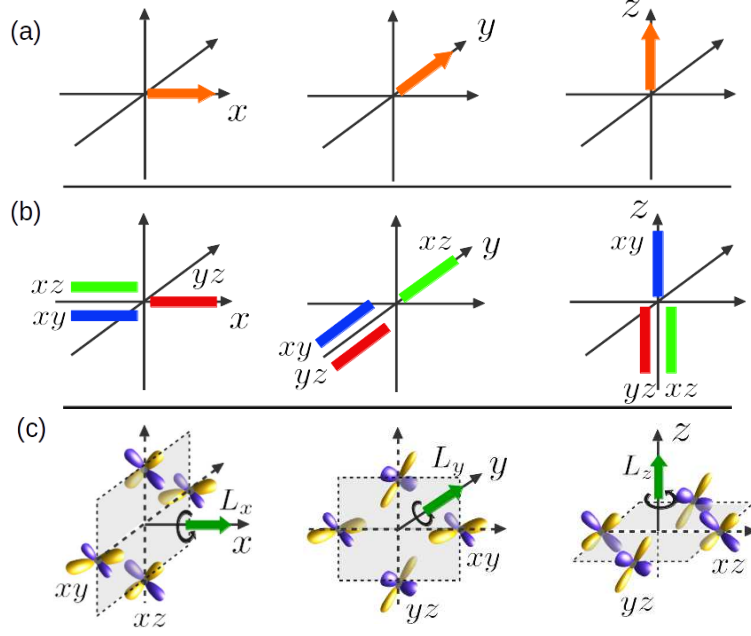


FIG. 12: The extreme spin-orbital-entanglement induced correspondence between (a) magnetic ordering directions, (b) sign of magnetic moments for the three orbitals, and (c) orbital current induced orbital moments for the three orbitals, for the $n = 5$ case corresponding to Sr_2IrO_4 .

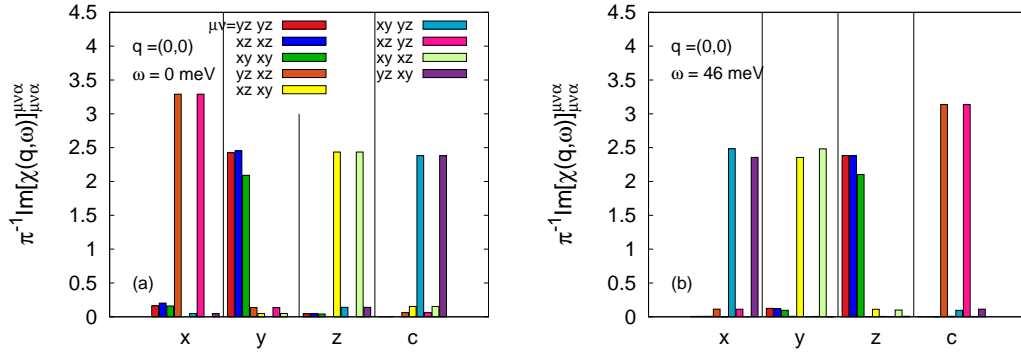


FIG. 13: The basis-resolved contributions to the total spectral function for the (a) gapless in-plane magnon mode and (b) gapped out-of-plane magnon mode for the $n = 5$ case corresponding to Sr_2IrO_4 with extreme spin-orbital entanglement.

Similarly, for the $n = 5$ case corresponding to Sr_2IrO_4 , the detailed spin-orbital character of the Goldstone mode and gapped mode at $\mathbf{q} = (0,0)$ seen in Fig. 6 is shown in Fig. 13, explicitly illustrating the effect of extreme spin-orbital entanglement and the resulting correspondence (Fig. 12) between magnetic ordering directions, spin moments, and orbital moments.

* Electronic address: avinas@iitk.ac.in

- ¹ W. Witczak-Krempa, G. Chen, Y. B. Kim, and L. Balents, *Correlated Quantum Phenomena in the Strong Spin-Orbit Regime*, Annu. Rev. Condens. Matter Phys. **5**, 57 (2014).
- ² J. G. Rau, E. Kin-Ho Lee, and H.-Y. Kee, *Spin-Orbit Physics Giving Rise to Novel Phases in Correlated Systems: Iridates and Related Materials*, Annu. Rev. Condens. Matter Phys. **7**, 195 (2016).
- ³ G. Cao and P. Schlottmann, *The Challenge of Spin-Orbit-Tuned Ground States in Iridates: A Key Issues Review*, Rep. Prog. Phys. **81**, 042502 (2018).
- ⁴ G. Zhang and E. Pavarini, *Spin-Orbit and Coulomb Effects in Single-Layered Ruthenates*, Phys. Status Solidi RRL **12**, 1800211 (2018).
- ⁵ J. Bertinshaw, Y. K. Kim, G. Khaliullin, and B. J. Kim, *Square Lattice Iridates*, Annu. Rev. Condens. Matter Phys. **10**, 315 (2019).
- ⁶ G. Zhang and E. Pavarini, *Higgs Mode and Stability of xy -orbital Ordering in Ca_2RuO_4* , Phys. Rev. B **101**, 205128 (2020).
- ⁷ Y. G. Shi, Y. F. Guo, S. Yu, M. Arai, A. A. Belik, A. Sato, K. Yamaura, E. Takayama-Muromachi, H. F. Tian, H. X. Yang, J. Q. Li, T. Varga, J. F. Mitchell, and S. Okamoto, *Continuous Metal-Insulator Transition of the Antiferromagnetic Perovskite NaOsO_3* , Phys. Rev. B **80**, 161104(R) (2009).
- ⁸ S. Calder, V. O. Garlea, D. F. McMorrow, M. D. Lumsden, M. B. Stone, J. C. Lang, J.-W. Kim, J. A. Schlueter, Y. G. Shi, K. Yamaura, Y. S. Sun, Y. Tsujimoto, and A. D. Christianson, *Magnetically Driven Metal-Insulator Transition in NaOsO_3* , Phys. Rev. Lett. **108**, 257209 (2012).
- ⁹ Y. Du, X. Wan, L. Sheng, J. Dong, and S. Y. Savrasov, *Electronic Structure and Magnetic Properties of NaOsO_3* , Phys. Rev. B **85**, 174424 (2012).
- ¹⁰ M.-C. Jung, Y.-J. Song, K.-W. Lee, and W. E. Pickett, *Structural and Correlation effects in the Itinerant Insulating Antiferromagnetic Perovskite NaOsO_3* , Phys. Rev. B **87**, 115119 (2013).
- ¹¹ I. Lo Vecchio, A. Perucchi, P. Di Pietro, O. Limaj, U. Schade, Y. Sun, M. Arai, K. Yamaura, and S. Lupi, *Infrared evidence of a Slater Metal-Insulator Transition in NaOsO_3* , Sci. Rep. **3**, 2990 (2013).

- ¹² B. Kim, P. Liu, Z. Ergönenc, A. Toschi, S. Khmelevskyi, and C. Franchini, *Lifshitz Transition Driven by Spin Fluctuations and Spin-Orbit Renormalization in NaOsO₃*, Phys. Rev. B **94**, 241113(R) (2016).
- ¹³ J. G. Vale, S. Calder, C. Donnerer, D. Pincini, Y. G. Shi, Y. Tsujimoto, K. Yamaura, M. Moretti Sala, J. van den Brink, A. D. Christianson, and D. F. McMorrow, *Evolution of the Magnetic Excitations in NaOsO₃ through its Metal-Insulator Transition*, Phys. Rev. Lett. **120**, 227203 (2018).
- ¹⁴ S. Mohapatra, C. Bhandari, S. Satpathy, and A. Singh, *Effect of Structural Distortion on the Electronic Band Structure of NaOsO₃ studied within Density Functional Theory and a Three-Orbital Model*, Phys. Rev. B **97**, 155154 (2018).
- ¹⁵ A. Singh, S. Mohapatra, C. Bhandari, and S. Satpathy, *Spin-Orbit Coupling Induced Magnetic Anisotropy and Large Spin Wave Gap in NaOsO₃*, J. Phys. Commun. **2**, 115016 (2018).
- ¹⁶ S. Calder, J. G. Vale, N. Bogdanov, C. Donnerer, D. Pincini, M. Moretti Sala, X. Liu, M. H. Upton, D. Casa, Y. G. Shi, Y. Tsujimoto, K. Yamaura, J. P. Hill, J. van den Brink, D. F. McMorrow, and A. D. Christianson, *Strongly Gapped Spin-Wave Excitation in the Insulating Phase of NaOsO₃*, Phys. Rev. B **95**, 020413(R) (2017).
- ¹⁷ J. G. Vale, S. Calder, C. Donnerer, D. Pincini, Y. G. Shi, Y. Tsujimoto, K. Yamaura, M. Moretti Sala, J. van den Brink, A. D. Christianson, and D. F. McMorrow, *Crossover from Itinerant to Localized Magnetic Excitations Through the Metal-Insulator Transition in NaOsO₃*, Phys. Rev. B **97**, 184429 (2018).
- ¹⁸ S. Nakatsuji, S.-i. Ikeda, and Y. Maeno, *Ca₂RuO₄: New Mott Insulators of Layered Ruthenate*, J. Phys. Soc. Jpn **66**(7), 1868 (1997).
- ¹⁹ M. Braden, G. André, S. Nakatsuji, and Y. Maeno, *Crystal and Magnetic Structure of Ca₂RuO₄: Magnetoelastic Coupling and the Metal-Insulator Transition*, Phys. Rev. B **58**, 847 (1998).
- ²⁰ C. S. Alexander, G. Cao, V. Dobrosavljevic, S. McCall, J. E. Crow, E. Lochner, and R. P. Guertin, *Destruction of the Mott Insulating Ground State of Ca₂RuO₄ by a Structural Transition*, Phys. Rev. B **60**, R8422 (1999).
- ²¹ O. Friedt, M. Braden, G. André, P. Adelmann, S. Nakatsuji, and Y. Maeno, *Structural and Magnetic Aspects of the Metal-Insulator Transition in Ca_{2-x}Sr_xRuO₄*, Phys. Rev. B **63**, 174432 (2001).
- ²² E. Gorelov, M. Karolak, T. O. Wehling, F. Lechermann, A. I. Lichtenstein, and E. Pavarini,

- Nature of the Mott Transition in Ca_2RuO_4* , Phys. Rev. Lett. **104**, 226401 (2010).
- ²³ G. Zhang and E. Pavarini, *Mott transition, Spin-Orbit Effects, and Magnetism in Ca_2RuO_4* , Phys. Rev. B **95**, 075145 (2017).
 - ²⁴ D. Sutter, C. G. Fatuzzo, S. Moser, M. Kim, R. Fittipaldi, A. Vecchione, V. Granata, Y. Sassa, F. Cossalter, G. Gatti, M. Grioni, H. M. Rønnow, N. C. Plumb, C. E. Matt, M. Shi, M. Hoesch, T. K. Kim, T.-R. Chang, H.-T. Jeng, C. Jozwiak, A. Bostwick, E. Rotenberg, A. Georges, T. Neupert, and J. Chang, *Hallmarks of Hund's Coupling in the Mott Insulator Ca_2RuO_4* , Nat. Comm. **8**, 15176 (2017).
 - ²⁵ F. Nakamura, T. Goko, M. Ito, T. Fujita, S. Nakatsuji, H. Fukazawa, Y. Maeno, P. Alireza, D. Forsythe, and S. R. Julian, *From Mott Insulator to Ferromagnetic Metal: A Pressure Study of Ca_2RuO_4* , Phys. Rev. B **65**, 220402(R) (2002).
 - ²⁶ P. Steffens, O. Friedt, P. Alireza, W. G. Marshall, W. Schmidt, F. Nakamura, S. Nakatsuji, Y. Maeno, R. Lengsdorf, M. M. Abd-Elmeguid, and M. Braden, *High-pressure Diffraction Studies on Ca_2RuO_4* , Phys. Rev. B **72**, 094104 (2005).
 - ²⁷ H. Taniguchi, K. Nishimura, R. Ishikawa, S. Yonezawa, S. K. Goh, F. Nakamura, and Y. Maeno, *Anisotropic Uniaxial Pressure Response of the Mott Insulator Ca_2RuO_4* , Phys. Rev. B **88**, 205111 (2013).
 - ²⁸ S. Nakatsuji and Y. Maeno, *Quasi-Two-Dimensional Mott Transition System $\text{Ca}_{2-x}\text{Sr}_x\text{RuO}_4$* , Phys. Rev. Lett. **84**, 2666 (2000).
 - ²⁹ Z. Fang and K. Terakura, *Magnetic Phase Diagram of $\text{Ca}_{2-x}\text{Sr}_x\text{RuO}_4$ Governed by Structural Distortions*, Phys. Rev. B **64**, 020509 (2001).
 - ³⁰ P. Steffens, O. Friedt, Y. Sidis, P. Link, J. Kulda, K. Schmalzl, S. Nakatsuji, and M. Braden, *Magnetic Excitations in the Metallic Single-Layer Ruthenates $\text{Ca}_{2-x}\text{Sr}_x\text{RuO}_4$ Studied by Inelastic Neutron Scattering*, Phys. Rev. B **83**, 054429 (2011).
 - ³¹ C. Dietl, S. K. Sinha, G. Christiani, Y. Khaydukov, T. Keller, D. Putzky, S. Ibrahimkuty, P. Wochner, G. Logvenov, P. A. van Aken, B. J. Kim, and B. Keimer, *Tailoring the Electronic Properties of Ca_2RuO_4 via Epitaxial Strain*, Appl. Phys. Lett. **112**, 031902 (2018).
 - ³² F. Nakamura, M. Sakaki, Y. Yamanaka, S. Tamaru, T. Suzuki, and Y. Maeno, *Electric-Field-Induced Metal Maintained by Current of the Mott Insulator Ca_2RuO_4* , Sci. Rep. **3**, 2536 (2013).
 - ³³ R. Okazaki, Y. Nishina, Y. Yasui, F. Nakamura, T. Suzuki, and I. Terasaki, *Current-Induced Gap Suppression in the Mott Insulator Ca_2RuO_4* , J. Phys. Soc. Jpn. **82**, 103702 (2013).

- ³⁴ S. Kunkemöller, D. Khomskii, P. Steffens, A. Piovano, A. A. Nugroho, and M. Braden, *Highly Anisotropic Magnon Dispersion in Ca_2RuO_4 : Evidence for Strong Spin-Orbit Coupling*, Phys. Rev. Lett. **115**, 247201 (2015).
- ³⁵ A. Jain, M. Krautloher, J. Porras, G. H. Ryu, D. P. Chen, D. L. Abernathy, J. T. Park, A. Ivanov, J. Chaloupka, G. Khaliullin, B. Keimer, and B. J. Kim, *Higgs Mode and Its Decay in a Two-Dimensional Antiferromagnet*, Nat. Phys. **13**, 633 (2017).
- ³⁶ S. Kunkemöller, E. Komleva, S. V. Streltsov, S. Hoffmann, D. I. Khomskii, P. Steffens, Y. Sidis, K. Schmalzl, and M. Braden, *Magnon dispersion in $\text{Ca}_2\text{Ru}_{1-x}\text{Ti}_x\text{O}_4$: Impact of Spin-Orbit Coupling and Oxygen Moments*, Phys. Rev. B **95**, 214408 (2017).
- ³⁷ S.-M. Souliou, J. Chaloupka, G. Khaliullin, G. Ryu, A. Jain, B. J. Kim, M. Le Tacon, and B. Keimer, *Raman Scattering from Higgs Mode Oscillations in the Two-Dimensional Antiferromagnet Ca_2RuO_4* , Phys. Rev. Lett. **119**, 067201 (2017).
- ³⁸ C. G. Fatuzzo, M. Dantz, S. Fatale, P. Olalde-Velasco, N. E. Shaik, B. Dalla Piazza, S. Toth, J. Pelliciani, R. Fittipaldi, A. Vecchione, N. Kikugawa, J. S. Brooks, H. M. Rønnow, M. Grioni, Ch. Rüegg, T. Schmitt, and J. Chang, *Spin-Orbit-Induced Orbital Excitations in Sr_2RuO_4 and Ca_2RuO_4 : A resonant Inelastic X-Ray Scattering Study*, Phys. Rev. B **91**, 155104 (2015).
- ³⁹ L. Das, F. Forte, R. Fittipaldi, C. G. Fatuzzo, V. Granata, O. Ivashko, M. Horio, F. Schindler, M. Dantz, Yi Tseng, D. E. McNally, H. M. Rønnow, W. Wan, N. B. Christensen, J. Pelliciani, P. Olalde-Velasco, N. Kikugawa, T. Neupert, A. Vecchione, T. Schmitt, M. Cuoco, and J. Chang, *Spin-Orbital Excitations in Ca_2RuO_4 Revealed by Resonant Inelastic X-Ray Scattering*, Phys. Rev. X **8**, 011048 (2018).
- ⁴⁰ H. Gretarsson, H. Suzuki, Hoon Kim, K. Ueda, M. Krautloher, B. J. Kim, H. Yavaş, G. Khaliullin, and B. Keimer, *Observation of Spin-Orbit Excitations and Hund's Multiplets in Ca_2RuO_4* , Phys. Rev. B **100**, 045123 (2019).
- ⁴¹ B. J. Kim, H. Jin, S. J. Moon, J.-Y. Kim, B.-G. Park, C. S. Leem, J. Yu, T. W. Noh, C. Kim, S.-J. Oh, J.-H. Park, V. Durairaj, G. Cao and E. Rotenberg, *Novel $J_{\text{eff}} = 1/2$ Mott State Induced by Relativistic Spin-Orbit Coupling in Sr_2IrO_4* , Phys. Rev. Lett. **101**, 076402 (2008).
- ⁴² B. J. Kim, H. Ohsumi, T. Komesu, S. Sakai, T. Morita, H. Takagi and T. Arima, *Phase-Sensitive Observation of a Spin-Orbital Mott State in Sr_2IrO_4* , Science **323**, 1329–1332 (2009).
- ⁴³ J. Kim, D. Casa, M. H. Upton, T. Gog, Y.-J. Kim, J. F. Mitchell, M. van Veenendaal, M. Daghofer, J. van den Brink, G. Khaliullin, and B. J. Kim, *Magnetic Excitation Spectra of Sr_2IrO_4*

- Probed by Resonant Inelastic X-Ray Scattering: Establishing Links to Cuprate Superconductors*, Phys. Rev. Lett. **108**, 177003 (2012).
- ⁴⁴ J-i Igarashi and T. Nagao, *Interplay between Hund's Coupling and Spin-Orbit Interaction on Elementary Excitations in Sr₂IrO₄*, J. Phys. Soc. Jpn. **83**, 053709 (2014).
- ⁴⁵ D. Pincini, J. G. Vale, C. Donnerer, A. de la Torre, E. C. Hunter, R. Perry, M. Moretti Sala, F. Baumberger, and D. F. McMorrow, *Anisotropic Exchange and Spin-Wave Damping in Pure and Electron-Doped Sr₂IrO₄*, Phys. Rev. B **96**, 075162 (2017).
- ⁴⁶ J. Porras, J. Bertinshaw, H. Liu, G. Khaliullin, N. H. Sung, J.-W. Kim, S. Francoual, P. Steffens, G. Deng, M. Moretti Sala, A. Effimenko, A. Said, D. Casa, X. Huang, T. Gog, J. Kim, B. Keimer, and B. J. Kim, *Pseudospin-Lattice Coupling in the Spin-Orbit Mott Insulator Sr₂IrO₄*, Phys. Rev. B **99**, 085125 (2019).
- ⁴⁷ S. Mohapatra, J. van den Brink, and A. Singh, *Magnetic Excitations in a Three-Orbital Model for the Strongly Spin-Orbit Coupled Iridates: Effect of Mixing Between the $J = 1/2$ and $3/2$ Sectors*, Phys. Rev. B **95**, 094435 (2017).
- ⁴⁸ J. Kim, M. Daghofer, A. H. Said, T. Gog, J. van den Brink, G. Khaliullin, and B. J. Kim, *Excitonic Quasiparticles in a Spin-Orbit Mott Insulator*, Nat. Commun. **5**, 4453 (2014).
- ⁴⁹ O. Krupin, G. L. Dakovski, B. J. Kim, J. Kim, S. Mishra, Yi-De Chuang, C. R. Serrao, W.-S. Lee, W. F. Schlotter, M. P. Minitti, D. Zhu, D. Fritz, M. Chollet, R. Ramesh, S. L. Molodtsov, and J. J. Turner, *Ultrafast Dynamics of Localized Magnetic Moments in the Unconventional Mott Insulator Sr₂IrO₄*, J. Phys.: Condens. Matter **28**, 32LT01 (2016).
- ⁵⁰ M. Souri, B. H. Kim, J. H. Gruenewald, J. G. Connell, J. Thompson, J. Nichols, J. Terzic, B. I. Min, G. Cao, J. W. Brill, and A. Seo, *Optical Signatures of Spin-Orbit Exciton in Bandwidth-Controlled Sr₂IrO₄ Epitaxial Films via High-Concentration Ca and Ba Doping*, Phys. Rev. B **95**, 235125 (2017).
- ⁵¹ S. Mohapatra and A. Singh, *Correlated Motion of Particle-Hole Excitations Across the Renormalized Spin-Orbit Gap in Sr₂IrO₄*, J. Magn. Magn. Mater **512**, 166997 (2020).
- ⁵² S. Mohapatra and A. Singh, *Magnetic Reorientation Transition in a Three Orbital Model for Ca₂RuO₄ — Interplay of Spin-Orbit Coupling, Tetragonal Distortion, and Coulomb Interactions*, J. Phys.: Condens. Matter **32**, 485805 (2020).
- ⁵³ S. Mohapatra and A. Singh, *Pseudo-Spin Rotation Symmetry Breaking by Coulomb Interaction terms in Spin-Orbit Coupled Systems*, J. Phys.: Condens. Matter **33**, 065802 (2021).

- ⁵⁴ G. Khaliullin, *Excitonic Magnetism in Van Vleck-type d^4 Mott Insulators*, Phys. Rev. Lett. **111**, 197201 (2013).
- ⁵⁵ A. Akbari and G. Khaliullin, *Magnetic Excitations in a Spin-Orbit-Coupled d^4 Mott Insulator on the Square Lattice*, Phys. Rev. B **90**, 035137 (2014).
- ⁵⁶ T. Feldmaier, P. Strobel, M. Schmid, P. Hansmann, and M. Daghofer, *Excitonic Magnetism at the Intersection of Spin-Orbit Coupling and Crystal-Field Splitting*, Phys. Rev. Research **2**, 033201 (2020).
- ⁵⁷ S. Mohapatra and A. Singh, *Spin Waves and Stability of Zigzag Order in the Hubbard Model with Spin-Dependent Hopping Terms: Application to the Honeycomb Lattice Compounds Na_2IrO_3 and $\alpha\text{-RuCl}_3$* , J. Magn. Magn. Mater **479**, 229 (2019).

